https://doi.org/10.5194/tc-2020-240
Preprint. Discussion started: 27 August 2020

The Cryosphere Discussions
Open Access
EGU

Modeling intensive ocean-cryosphere interactions in Lützow-Holm Bay, East Antarctica

Kazuya Kusahara[1], Daisuke Hirano[2, 3], Masakazu Fujii[4, 5], Alexander D. Fraser[6], Takeshi Tamura[4, 5]

[1]Japan Agency for Marine-Earth Science and Technology (JAMSTEC), Yokohama, Kanagawa, 236-0001, Japan
[2]Institute of Low Temperature Science, Hokkaido University, Sapporo, Hokkaido, 060-0819, Japan
[3]Arctic Research Center, Hokkaido University, Sapporo, Hokkaido, 001-0021, Japan
[4]National Institute of Polar Research, Tachikawa, Tokyo, 190-8518, Japan
[5]Graduate University for Advanced Studies (SOKENDAI), Tachikawa, Tokyo, 190-8518, Japan
[6]Australian Antarctic Program Partnership, University of Tasmania, Hobart, Tasmania, 7004, Australia

Correspondence to: Kazuya Kusahara (kazuya.kusahara@gmail.com, kazuya.kusahara@jamstec.go.jp)

https://doi.org/10.5194/tc-2020-240
Preprint. Discussion started: 27 August 2020

The Cryosphere Discussions
Open Access
EGU

Abstract. Basal melting of Antarctic ice shelves accounts for more than half of the mass loss from the Antarctic Ice Sheet. Many studies have focused on active basal melting at ice shelves in the Amundsen-Bellingshausen Seas and the Totten Ice shelf, East Antarctica. In these regions, the intrusion of Circumpolar Deep Water (CDW) onto the continental shelf is a key component for the localized intensive basal melting. Both regions have a common oceanographic feature: southward deflection of the Antarctic Circumpolar Current on the eastern flank of ocean gyres brings CDW onto the continental shelves. The physical setting of Shirase Glacier Tongue (SGT) in Lützow-Holm Bay corresponds to a similar configuration for the Weddell Gyre in the Atlantic sector. Here, we conduct a 2-3 km resolution simulation of an ocean-sea ice-ice shelf model using a newly-compiled bottom topography dataset in the bay. The model can reproduce the observed CDW intrusion along the deep trough. The modeled SGT basal melting reaches a peak in summer and minimum in autumn and winter, consistent with the wind-driven seasonality of the CDW thickness in the bay. The model results suggest the existence of eastward-flowing undercurrent on the upper continental slope in summer, and the undercurrent contributes to the seasonal-to-interannual variability of the warm water intrusion into the bay. Furthermore, numerical experiments with and without fast-ice cover in the bay demonstrate that fast ice plays a role as an effective thermal insulator and reduces local sea-ice formation, resulting in much warmer water intrusion into the SGT cavity.

https://doi.org/10.5194/tc-2020-240
Preprint. Discussion started: 27 August 2020

1 Introduction

The Antarctic ice sheet is the greatest freshwater reservoir on the present-day's Earth surface, most of which sits upon bedrock. The exchanges of the mass, heat, and freshwater between the Antarctic ice sheet and the ocean has played a critical role in regulating the global sea level and influencing the Earth's climate (Convey et al., 2009; Turner et al., 2009). Recent satellite observations have revealed a declining trend in the Antarctic ice sheet mass (Paolo et al., 2015; Rignot et al., 2011, 2019). Several observational and modeling studies have pointed out that enhanced intrusions of warm waters onto some Antarctic continental shelf regions trigger more active ocean-ice shelf interaction, leading to the negative mass balance of the Antarctic ice sheet. In this context, much attention has been paid to ocean-cryosphere interaction, particularly Antarctic ice shelf basal melting, which is the primary ablation process for the Antarctic ice sheet mass balance (Depoorter et al., 2013; Rignot et al., 2013).

Circumpolar Deep Water (CDW) is the warmest water mass at intermediate depths at all longitudes over the Southern Ocean, and the intrusions onto the Antarctic continental shelf regions result in the very active basal melting at the Antarctic ice shelves. Jacobs et al. (1996), in the first in-situ oceanographic observation in front of the Pine Island Glacier, reported that an intrusion of the CDW onto the Amundsen continental shelf provides large heat flux to melt the ice shelf base. After that time, many studies have shown evidence for active basal melting at the ice shelves in the Pacific sector (Jenkins et al., 2018), and the ice shelves in this sector have been well studied, along with the local bottom topography and the surrounding oceanic conditions.

More recently, several studies have started to focus on the Totten Ice shelf, Wilkes Land, East Antarctica, as a newly-recognized hot spot of active ice shelf-ocean interaction caused by a CDW intrusion (Rintoul et al., 2016; Silvano et al., 2016, 2018, 2019). Ice shelves in the Amundsen and Bellingshausen Seas and the Totten ice shelves have a common feature: the Antarctic Circumpolar Current (ACC) is proximal to the Antarctic coastal margins, and thus the CDW can affect regional coastal water masses. The Southern Ocean has three large-scale cyclonic (subpolar) gyres: Ross, Kerguelen, and Weddell Gyres (Gordon, 2008). Amundsen and Bellingshausen Seas and the offshore region of Wilkes Land correspond to south-eastern sides of the Ross and Kerguelen Gyres, respectively, where the southward flow of the large-scale ocean gyres brings warm water poleward to the Antarctic coastal margins (Gille et al., 2016). By analogy to the relationship between the two gyres and the active ice shelf melting areas, one can naturally speculate active ocean-ice shelf interaction around the south-eastern side of the Weddell Gyre. In fact, looking at an estimate of basal melt rate from Rignot et al. (2013), such a glacier tongue exhibits a high basal melt rate of 7±2 m yr^{-1}, although it areal extent is small. This glacier, Shirase Glacier in Lützow-Holm Bay (LHB), Enderby Land, East Antarctica, is one of the fastest flowing glaciers around Antarctica (Nakamura et al., 2010; Rignot, 2002).

The coastal Japanese Antarctic station, Syowa Station, is located within LHB, and it is the main platform of the Japanese Antarctic Research Expedition (JARE) for Japanese Antarctic sciences. LHB is bounded to the east by the north-south oriented coastline and to the west by northwest-southeast coastline/ice shelf (Fig. 1), and the semi-closed bay is open to the north. As an interesting feature, LHB is usually covered with multi-year fast ice throughout the year (Fraser et al., 2012, 2020; Nihashi and Ohshima, 2015; Ushio, 2006). The fast-ice cover has made in-situ oceanographic observations difficult. Notably, JARE (31st and 32nd expeditions from 1990 to 1992) conducted year-round oceanographic observations through drilled holes on the fast ice in LHB. Ohshima et al. (1996) analyzed these observation data and investigated the seasonal cycle of Winter Water (WW), which is surface-to-subsurface cold water formed in a winter mixed layer. Furthermore, they proposed a physical mechanism of seasonal change in the WW thickness: the strength of the alongshore wind stress controls the WW thickness through Ekman convergence. At that time, although the study did not focus on warm water near the

https://doi.org/10.5194/tc-2020-240
Preprint. Discussion started: 27 August 2020

bottom, their ocean observations in the bay clearly show the presence of CDW (characterized by high temperatures > 0.0°C, and high salinity > 34.5 psu) below the WW (characterized by the near surface-freezing temperatures). Stronger winds in autumn and winter increase Ekman convergence, thickening the WW in the surface to subsurface layers and thinning a warm water layer below the WW. Conversely, weaker winds in the summer season relax the Ekman convergence, leading to a relatively thin WW layer and a thicker CDW layer in deep layers.

Although multi-year fast ice usually covers the southern part of LHB, the fast ice has experienced extensive breakup events with irregular intervals of a few decades (Aoki, 2017; Ushio, 2006). A relatively large breakup occurred from March to April 2016. As a result of the breakup event, 58th JARE could perform an extensive campaign of trans-bay ship-based hydrographic observations to investigate possible ocean-ice shelf/glacier interaction in LHB (Hirano et al., 2020). The in-situ oceanographic observations in the bay elucidate intrusion of CDW onto the continental shelf, and the warm-water signal extends to the front of the SGT, indicating active ice-ocean interaction at SGT.

As mentioned above, LHB and SGT appear to be a suitable place for examining Antarctic ocean-ice shelf interaction in the Atlantic sector. However, they have been overlooked until very recently. Although the recent oceanographic observations show the existence of CDW in the bay (Hirano et al., 2020), little is known about the variability of the warm water intrusions, and it is not clear how the intrusion is controlled. As far as we know, there is no numerical modeling study that focuses on the water mass formation/exchange and the ocean-ice shelf interaction in this region. In this study, we perform a numerical simulation to illustrate coastal water masses and ocean-ice shelf interaction in LHB. In particular, we focus on the seasonal-interannual variability of warm water intrusion from shelf break to the bay and basal melting at SGT. Additionally, we investigate the roles of fast ice on ocean conditions and the ice-ocean interaction in this area.

2 Numerical model, bottom topography, and atmospheric conditions

2.1 An ocean-sea ice-ice shelf model for Lützow-Holm Bay

This study utilized a coupled ocean–sea ice–ice shelf model (Kusahara and Hasumi, 2013, 2014). The model employed an orthogonal, curvilinear, horizontal coordinate system. Two singular points of the horizontal curvilinear coordinate in the model were placed on the East Antarctic continent (72°S, 30°E and 69°S, 50°E) to regionally enhance the horizontal resolution around the LHB region while keeping the model domain circumpolar Southern Ocean. An artificial northern boundary was placed at approximately 30°S. The same technique to enhance the regional horizontal resolution has been used for several studies on Antarctic coastal ocean modeling (Kusahara et al., 2010, 2017; Marsland et al., 2004, 2007).

The vertical coordinate system of the ocean model was z coordinates. There are four vertical levels of 5-m cell thickness below the ocean surface, and 49 levels of 20-m thickness in the depth range from 20 m to 1000 m. Below this depth, the vertical spacing varies with depth (50-m thickness for 1000-2000 m, 100-m thickness for 2000-3000 m, and 200-m thickness for 3000-5000 m). The maximum ocean depth in the model was set to 5000 m to save computational resources. The model has an ice shelf component for the z-coordinate system (Losch, 2008). A partial step representation was adopted for both the bottom topography and ice shelf draft to represent them optimally in the z-coordinate ocean model (Adcroft et al., 2002). The sea-ice component used one-layer thermodynamics (Bitz and Lipscomb, 1999) and a two-category ice thickness representation (Hibler, 1979). Prognostic equations for momentum, mass, and concentration were taken from Mellor and Kantha (1989). Internal ice stress was formulated by the elastic-viscous-plastic rheology (Hunke and Dukowicz, 1997), and sea ice salinity was fixed at 5 psu.

https://doi.org/10.5194/tc-2020-240
Preprint. Discussion started: 27 August 2020


The Cryosphere Discussions

In the ice shelf component, we assumed a steady shape in the horizontal and vertical directions. The freshwater flux at the base of ice shelves was calculated with a three equation scheme, based on a pressure-dependent freezing point equation and conservation equations for heat and salinity (Hellmer and Olbers, 1989; Holland and Jenkins, 1999). We used the velocity-independent coefficients for the thermal and salinity exchange velocities (i.e., $\gamma_t = 1.0 \times 10^{-4}$ m s^{-1} and $\gamma_s = 5.05 \times 10^{-7}$ m s^{-1}, Hellmer and Olbers (1989)), although ocean velocity-dependent coefficients have been often used in the recent ice shelf-ocean modeling studies. Velocity magnitudes under the ice shelves strongly depend on the horizontal and vertical grid resolutions (Gwyther et al., 2020), we preferred using the velocity-independent version to minimize the dependency originated from the model configuration. The modeled meltwater flux and the associated heat flux were imposed on the ice shelf–ocean interface.

The horizontal grid spacing over the LHB region was less than 2.5 km (Fig. 1). This relatively high horizontal resolution enabled us to accurately reproduce coastline, ice front line, and bottom topography in the focal region. The background bathymetry for the Southern Ocean in this model was derived from the ETOPO1 (Amante and Eakins, 2009), while the ice shelf draft and bathymetry under the ice shelf were obtained from the RTopo-2 dataset (Schaffer et al., 2016). The bottom topography in the LHB bay region (35-40°E, and 70-68°S) was replaced with a detailed topography that blended multi-beam surveys from the 51st-55th JARE expeditions, point echo sounding using sea ice drill holes from the 9th-22nd JARE expeditions (Moriwaki and Yoshida, 1983), depth data from the nautical chart created by Japan Coast Guard (JCG), in which ship-based single-beam echo sounding data obtained in several JARE expeditions were included, and ETOPO1 (Amante and Eakins, 2009). The detail for the compiled bottom topography was described in the Method section in Hirano et al. (2020). In a later subsection 2.3, we compare the newly-compiled bottom topography with several topography datasets.

As mentioned in the introduction, extensive fast ice has been identified along the East Antarctic coast (Fraser et al., 2012; Nihashi and Ohshima, 2015), and the existence of persistent fast ice characterizes LHB. We introduced areas of multi-year fast ice cover into LHB in the model as constant-thickness (5 m) ice shelf grid cells. Although, in reality, the horizontal distribution and thickness of fast ice vary seasonally and interannually (Aoki, 2017; Fraser et al., 2012; Ushio, 2006), the spatial distribution of multi-year fast ice in the model was assumed to be constant in time as a first approximation. This assumption is likely more valid here in LHB than in more dynamic areas of fast ice cover, where breakouts can occur many times per year. The fast ice in the model prohibits momentum, heat, and freshwater fluxes at the ocean surface with atmosphere. Since the fast ice in the model is treated as thin ice-shelf, the fast ice also provides freshwater to the ocean surface, based on the melt rate diagnosed with thermodynamic fast ice-ocean interaction.

The model's initial conditions of temperature and salinity were derived from the Polar Science Center Hydrographic Climatology (Steele et al., 2001), with zero ocean velocity over the model domain. Note that the water properties in the climatology over the Southern Ocean come from World Ocean Atlas 1998 (Conkright et al., 1999). North of 40°S, ocean temperature and salinity were restored to the monthly mean climatology throughout the water column with a damping time scale of 10 days. Outside of the focal region where the horizontal resolution becomes coarser than 10 km, sea surface salinity was restored to the monthly mean climatology to suppress unrealistic deep convection in some regions (e.g., the Weddell Sea).

Daily surface boundary conditions for the model were surface winds, air temperature, specific humidity, downward shortwave, downward longwave, and freshwater flux. To calculate the wind stress and sensible and latent heat fluxes, we used the bulk formula of Kara et al. (2000). When the surface air temperature was below 0°C, precipitation was treated as

https://doi.org/10.5194/tc-2020-240
Preprint. Discussion started: 27 August 2020

snow. Daily reanalysis atmospheric conditions were calculated from the ERA-Interim dataset (Dee et al., 2011). The ocean-sea ice-ice shelf model was first integrated for 20 years with the 2005-year forcing for spin-up to obtain a quasi-steady state in the ocean and cryosphere components.

We performed three experiments: "CKDRF", "FI", and "NOFI" cases. All three experiments started from the final state of the spin-up integration. The effect of fast ice is included in the first two experiments (CKDRF and FI cases), but not in the NOFI case. In the CKDRF case, the model is continued to be driven by the 2005-year surface forcing to check a model drift in the experiments. In the FI and NOFI cases, a hindcast simulation was carried out for the period 2006-2018 with interannually varying forcing. The difference between the FI and NOFI cases allows us to examine the role of fast ice on the ocean and cryosphere components. It should be noted that the two icescape configurations were largely simplified compared to the actual time-varying fast ice distribution. The numerical results from the two extreme cases were utilized to purely estimate the impact of the fast ice.

2.2 Bottom topography in Lützow-Holm Bay

The accuracy of bottom topography is critically vital for high-resolution ocean modeling because the geostrophic contour/bottom topography strongly controls ocean flows (including CDW intrusions on the East Antarctic continental shelf, e.g., Nitsche et al. (2017)) and the associated water properties. Several large-scale compilations of bottom topography are now available. As an example, Figure 2b-f shows spatial distributions of bottom topography in our focal region in five bottom topography datasets: ETOPO1 (Amante and Eakins, 2009), ETOPO5 (NOAA, 1988), GEBCO (IOC, IHO and BODC, 2003), RTopo-1 (Timmermann et al., 2010), and RTopo-2 (Schaffer et al., 2016). As can be seen in Fig 2, there are considerable differences in the representations of bottom topography, in particular in the southern half of LHB where fast ice is particularly present. All of the products have a sill-like feature at around 37.0°E and 68.4°S and depression-like features south of it. In the five products, ETOPO1 captures the large-scale features when comparing with JARE's in-situ depth observations (see dots in Fig 2a). For this reason, we used the ETOPO1 dataset for the background topography for our newly-compiled topography.

Looking at the newly-compiled topography, there are two submarine canyons on both sides of the sill at the latitudes of 68.4°S. It should be noted that the bathymetric features around the sill, including the submarine canyons, are well constrained by the observed depths derived from the point echo sounding and the hydrographic chart (colored dots in Fig. 2a). Acoustically observed data confirms that the sill top is ~500 m deep and surrounded by at least ~850 m deep western submarine canyon and 1600 m deep eastern submarine canyon. South of the sills, there is a large depression whose maximum depth is deeper than 1000 m. From the depression, four troughs are extended southward. The most eastern tough (labeled with T4) is the longest and deepest among them and extends toward SGT. In the southern part of the trough, there is a north-southward elongated depression at the latitudes from 69.5°S to 70°S. The feature is confirmed in the observational data; relatively 400 m deeper trough with the floor depth of ~850 m at 69.1°S and relatively 1200 m deeper trough with the floor depth of ~1600 m at 69.8°S. A direct comparison with JARE's in-situ measurement (Fig. 2a) provides assurance that the newly-compiled dataset is the best estimate of bottom topography in the LHB region at this moment.

2.3 Atmospheric conditions

In this subsection, we show seasonal changes in the long-term mean fields of mean sea level pressure (MSLP) over the Southern Ocean and surface winds off the LHB region (Fig. 2), based on the ERA-Interim climatology for the period 1979-

https://doi.org/10.5194/tc-2020-240
Preprint. Discussion started: 27 August 2020

2018. A circumpolar pattern of low pressure at high southern latitudes and high pressure at lower latitudes accompanies a prevailing westerly wind over the Southern Ocean in the latitudes from 40°S to 60°S, being a predominant spatial pattern in the high-latitudes Southern Hemisphere. There are three regional minimums of the MSLP in the Weddell Sea, the Indian Sector, and the Amundsen Sea, and the regional minimums deepen in the autumn and winter seasons. South of the air pressure minimums (i.e., Antarctic coastal regions) is a prevailing easterly wind regime, which is the driving force of westward flowing currents along the Antarctic coastal margins (Thompson et al., 2018).

LHB is located on the south-eastern side of the low pressure in the Weddell Sea (see the red box in Fig. 3). In the longitude bands, the westerly wind blows north of 62°S, and the easterly wind blows south of 64°S throughout a year (Fig. 3e-h). The alongshore component dominates the easterly wind, and the wind speed reaches the maximum from April to June and the minimum in the spring and summer seasons (from October to January). Ohshima et al. (1996) pointed out that the seasonal change in the alongshore wind controls the seasonality of the surface WW thickness in LHB (i.e., thickening in autumn and winter and thinning in spring and summer).

3 Warm water intrusion into LHB and active basal melting at Shirase Glacier Tongue

Since the model started from a motionless state with the climatological ocean properties, it requires a spin-up time to adjust simulated ocean circulation and water masses in LHB to a quasi-steady state. In this study, we can use the time series of the basal melt rate at SGT to monitor the spin-up of the ocean-cryosphere system in LHB (Fig. 4) because the basal melting is an integrated result from the interaction between the ocean flow and coastal water masses. As can be seen in Fig. 4a, the basal melt rate reaches a quasi-steady state after approximately 20-year. There is a slightly declining trend in the basal melt rate after the 20-year spin-up, due to an inherent model drift or insufficient spin-up for the circumpolar Southern Ocean. However, the magnitude of the declining trend of the melt rate in the CKDRF case is much smaller than interannual variability and the difference between the NOFI and FI cases (Fig. 5a). Therefore, we can use the results from the NOFI and FI cases to examine the seasonal and interannual variability and the difference between the experiments.

3.1 Intrusion of modified Circumpolar Deep Water into LHB

In this section, we use results from the NOFI case to validate the modeled ocean fields because the in-situ observation in 2017 January after the extensive breakup of multi-year fast ice in austral autumn of 2016 (Aoki, 2017). The monthly climatology for the modeled fields was calculated by averaging the variables over the period 2008-2018. The model results in the first two years 2006-2007 were excluded in the calculation due to a transition from the sudden removal of the fast ice cover in the NOFI case. Figure 6 shows the spatial distribution of the modeled bottom temperature in January with two observational sections (TROUGH section and A-line). The TROUGH section is a north-southward running observational line from the deep depression to the SGT ice front, and the A-line is located at approximately 69.58°S. Warm water intrusions into LHB from the shelf break are clearly seen in Fig. 6, and the warmest waters are identified along the four troughs (T1, T2, T3, and T4 from west to east). Warm water in the trough T4 (e.g., along the TROUGH section) extends southward toward SGT and Skallen Glacier (SkG).

The vertical profile of the ocean properties along the TROUGH section is a clear two-layer structure consisting of a cold-fresh surface layer and a warm-saline deep layer (Fig. 7). Colored circles in Fig. 7 are subsampled ocean properties from the in-situ observations (Hirano et al., 2020). The two-layer feature in the model is consistent with the observation results. In

https://doi.org/10.5194/tc-2020-240
Preprint. Discussion started: 27 August 2020

particular, the model can reasonably represent the inflowing warm water temperature in the bottom layer along the trough. The temperature of the warm water intrusion is much warmer than the local freezing point and thus a driver of high basal melting at SGT. However, there are some model biases in salinity. The observed salinity near the bottom throughout the section is higher by more than 0.1 psu than in the model. Since the less saline signal in the model is found near the sill region, the salinity biases probably come from an insufficient representation of salinity values on the continental shelf slope and rise regions.

The vertical section of potential temperature along the A-line with the normal velocity (positive for northward) illustrates that the warm water intrusion is strongly trapped near the bottom on the eastern flank of the deep trough (Fig. 8). In January, the warm water (> 0°C) is present in the bottom layer denser than 27.6 kg m^{-3}, and the magnitude of the southward flow is larger than 10 cm s^{-1} (Fig. 8a). On the western side of the trough, northward flow of cold and fresh water is reproduced at the surface and intermediate depths. The overturning circulation in the model is generally consistent with that inferred from the observed water properties (temperature, salinity, oxygen, and the stable oxygen isotope ratio, $\delta^{18}O$, Hirano et al., 2020). These patterns of the ocean properties and circulation are persistent throughout the year, but with a smaller magnitude of the warm water intrusion in autumn and winter (Fig. 8b).

In order to identify locations of the warm water intrusions from the offshore region to LHB, we show vertical profiles of the potential temperature, potential density, and north/southward ocean flow along the sill section at the latitude of 68.5°S (Fig. 9). There are two submarine canyons in the section (we call the western and eastern canyons as “WC” and “EC”, respectively). Looking at the deep layers denser than 27.6 kg m^{-3}, southward flows are present in the two submarine canyons and bring very warm water (up to 1°C) into LHB. The southward ocean flow in the WC is stronger than that in the EC in summer (Fig. 9a for January), and these become comparable to each other in winter (Fig. 9b for July). In contrast, there is a strong northward flow of less dense/cold water in the surface layers on the western flank of the WC.

3.2 Basal melting at SGT

The warm water intrusion along the eastern flank of the deep trough results in a high basal melt rate at SGT (Fig. 6). Active basal melting with the annual melt rate higher than 10 m yr^{-1} is represented in the northern part of the SGT, where the warm water contacts first the SGT base. The southern part also has a high basal melt at approximately 5 m yr^{-1}. Since the circumpolar-averaged basal melt rate of the Antarctic ice shelves was estimated to be in a range from 0.81 to 0.94 m yr^{-1} (Depoorter et al., 2013; Rignot et al., 2013), we can conclude that SGT is a hot spot of ocean-ice shelf/glacier interaction caused by the CDW intrusions across the shelf break.

Next, we examine the relationship of the seasonal cycles between the water mass transport into the SGT cavity and the monthly basal melt rate at SGT (Fig. 10). We calculated the inflow transport of water masses exactly across the SGT ice front and the mean temperature in potential density bins with an interval of 0.02 kg m^{-3}. In this section, we focus on the results in the NOFI case to capture the seasonal cycles (Fig. 10a), while we examine in detail the difference between the NOFI and FI cases in a later section. Relatively warm water with temperatures higher than −0.5°C is present in the denser classes throughout the year, and the transport of the warm waters into the cavity reaches a maximum in summer (from November to February). The temperature of the inflowing water masses starts to decrease in March, and the total inflow volume transport declines in autumn and winter, leading to a rapid decrease in ocean heat flux into the SGT cavity. Consistent with the seasonal cycle of the warm water intrusion, SGT shows a substantial seasonal variation of the basal melt rate from 6 m yr^{-1} in winter to 13 m yr^{-1} in summer. It should be noted again that the melt rate in winter is still much higher

https://doi.org/10.5194/tc-2020-240
Preprint. Discussion started: 27 August 2020

than the circumpolar-averaged basal melt rate. The high basal melt rate throughout the year is caused by the persistent warm water intrusion in the deep layer in the LHB region.

Hirano et al. (2020) used an ice radar of autonomous phase-sensitive radio echo sounder (ApRES) to estimate basal melt rate at SGT for the period from February-2018 to January-2019 (green line in Fig. 5). Here, we briefly compare the seasonality of the SGT basal melt rates between the model result and the observation-based estimate. The model and observation both show the high basal melting rate in summer and the relatively low melt rate in autumn and winter (Fig. 5). The model can reproduce the rapid increase in the SGT basal melt rate from September to December. These general agreements provide some confidence for the model results in this study, especially for the seasonality of the SGT basal melt rate. However, there are some notable differences between the model and observations. The observed melt rate decreased rapidly from 10 m yr^{-1} in February-2018 to less than 1 m yr^{-1} in mid-March-2018. This reduction in the basal melt rate is outside of the model interannual variability. The discrepancy between the model and observation may come from either a limitation of the observation, the model approximation, or both. The observed estimate from the single location includes the entire SGT variability and regional variability. At this moment, it is not clear how much the single observation represents the entire SGT variability. In the model limitation, since the fast ice has interannual variability, the model results with the approximation of the steady-shape fast ice may be insufficient to capture the actual time series in the SGT basal melt rate in a transient icescape.

3.3 Warm water intrusions from the continental shelf break and slope regions to LHB

The previous analyses in this section demonstrated that the warm water intrusions onto the continental shelf extensively control the ocean structure in LHB, the water masses flowing into the SGT cavity, and the magnitude of the SGT basal melting (Figs. 6-10). Here, we examine the ocean temperature in the deep depression of the bay and ocean flow on the continental shelf and upper slope regions to explore water mass exchanges through the submarine canyons. A control box was defined just south of the sill on the shelf break to estimate the seasonal cycle of ocean temperature and density profiles (Fig. 11). The box encompasses the observation station G3 (Fig. 6). As shown in the previous figures (Figs. 7-9), there is relatively warm water in the deep layer below the cold surface layer. The two-layer structure persists throughout the year in the mouth of the bay. The potential density surface of 27.6 kg m^{-3} fluctuates at approximately 500-m depth, with a shoaling in summer and a deepening in autumn and winter. This seasonal cycle of the density surfaces in the box area is explained by the seasonality of the alongshore wind (Fig. 3, Hirano et al., (2020), and Ohshima et al. (1996)). Note that the seasonal cycle in the FI case is more apparent than that in the NOFI case because the fast ice cover plays a role as a physical barrier for the surface momentum flux and the wind stress curl input caused by the combination of fast ice edge and the alongshore easterly wind result in pronounced Ekman downwelling in this region (Ohshima, 2000).

Next, we show the spatial distribution of ocean flows at the surface and 500 m depth to identify the origin of the warm water mass flowing to LHB through the submarine canyons (Fig. 12). South-westward flows along the continental shelf slope predominate surface flows throughout the year. This alongshore surface flow is strong in winter and weak in summer (Figs. 12a and 12c), which corresponds to the seasonality of surface wind magnitude in this region (Fig. 3i). Ocean flow patterns at 500-m depth are quite different from the surface flow patterns. In summer, a strong eastward flow is produced on the continental slope between the 500-m and 2000-m isobaths. In this study, we use the term “undercurrent” to point out the eastward flow below the westward surface flow. A part of the undercurrent is redirected southward at the submarine canyons. The southward flow brings warm water in the deep layer into LHB (Fig. 12b, see also Figs. 9a and 11). On the other hand, in the winter, the undercurrent almost disappears, and the direction of the subsurface flow on the continental slope becomes

https://doi.org/10.5194/tc-2020-240
Preprint. Discussion started: 27 August 2020

westward, which is the same directions of the surface flow and the wind. Also, in the winter, a part of the westward subsurface flow is redirected southward at the submarine canyons, bringing warm water into the inside of the bay (Fig. 12d, see also Fig. 9b).

In order to examine the detailed characteristics of the undercurrent on the upper continental slope, vertical profiles of ocean temperature, density, and east-westward flow along a section at 35.75°E (see the black line in Fig. 12) are plotted in Figure 13. It should be noted that positive value in the current indicates westward flow to be consistent with flow direction in other figures (i.e., positive values for direction into the paper). In January, the surface-intensified westward flow is present in the depth range from the surface to 400 m, with the maximum speed larger than 6 cm s^{-1}. The eastward-flowing undercurrents locate in just offshore of the surface flow core in the depth range from 200 m to 1000 m (in the potential density range from 27.5 kg m^{-3} to 27.75 kg m^{-3}), and the maximum speed is approximately 6 cm s^{-1}. The undercurrent is attached at the bottom of the upper continental slope in the water depth from 500 m to 700 m. Again, in July, the undercurrent almost disappears, and the surface-intensified westward flow becomes more vigorous, extending the thickness to 1000-m depth. Figure 14a shows the seasonal variation of the eastward undercurrent transport across the section. In the NOFI case, the transport reaches the maximum in the summer season from January to March and the minimum in the autumn and winter seasons from May to September. In summary, the eastward-flowing undercurrent on the upper continental slope is the most developed during the summer months (Fig. 14a) when the easterly coastal winds are weakest (Fig. 3i).

4 Impacts of the fast ice on the ocean conditions and the SGT basal melting

Fast ice is formed by sea ice fastening to the Antarctic coastline and/or ice-shelf front, and the typical thickness is a few meters (Fraser et al., 2012; Giles et al., 2008). Note again that the fast ice in this model is represented as an uppermost-one-grid ice shelf. Fast ice becomes a physical barrier between ocean and atmosphere, modifying the exchanges of surface heat, freshwater, and momentum fluxes. The southern half of LHB is usually covered with fast ice, except during the breakup events. In this section, we examine the effects of the fast ice cover on the ocean conditions in LHB and explore the impact on the SGT melting, based on a comparison of results from the two experiments (NOFI and FI cases).

The ocean temperature difference along the TROUGH section between the two experiments (FI-NOFI) shows that fast ice plays a vital role in modifying the coastal water mass structure in the LHB region (Fig. 15). In this comparison, we used the climatological values in September when cold water formation associated with sea-ice formation (particularly in the NOFI case) was the most developed in LHB. There is a pronounced positive anomaly in the fast ice-covered region (e.g., south of the G3 station) throughout the year and the section, and significant differences are found in the depth range from the surface to 400 m. This result indicates that the coastal waters in the FI case are warmer than those in the NOFI case. The temperature difference in winter is more prominent than that in summer. In the deep layer from 400 m to the bottom, there are almost zero (but small negative) differences, resulting from warm water intrusions both in the NOFI and FI cases. It should be noted that judging from the melt rate difference in the two experiments (Fig. 4), the difference of the water properties in LHB is stable after approximately two years from the start of the NOFI and FI cases.

The annual mean basal melt rates at SGT in the NOFI and FI cases are 8.8 m $yr^{-1}$and 15.2 m yr^{-1}, respectively, and the melt rate difference is larger than the interannual variability (Fig. 5). Figure 10 clearly shows that the coastal water masses flowing into the SGT cavity in the FI case are much warmer than those in the NOFI case, although the seasonal cycle of the potential density surface in the deep layer (see green dots in Fig. 10) is similar in the two cases, as also inferred from Fig. 15.

https://doi.org/10.5194/tc-2020-240
Preprint. Discussion started: 27 August 2020

The water temperature in the FI case is warmer than -1.0°C throughout the year, while the water temperature of the intermediate-depth inflow in the NOFI case is lower than -1.0°C from March to September, as shown in blue colors in Fig. 10. The difference in the ocean heat transport into the SGT cavity causes a large difference in the modeled basal melt rates. Moreover, in the FI case, the fast ice base is also melted by the ocean. The annual mean basal melt rate over the fast ice in LHB is 2.3 m yr^{-1} in this model configuration, and the fast ice melt rate is much lower than the SGT melt rate. However, the areal extent of the fast ice is larger than the SGT's area, and thus melting fast ice is a pronounced freshwater source in the LHB region in the FI case (SGT: 7.8 Gt yr^{-1}; fast ice: 40.7 Gt yr^{-1}). In the FI case, a combination of the more active basal melting at SGT and the melting of fast ice provide the surplus surface freshwater in the southern part of LHB. Here, we comment on the feasibility of the modeled basal melt rate of the fast ice in the FI case. The mean melt rate over the fast ice in the model is higher than the climatological average precipitation of about 60 cm water equivalent per year (1979–2018 average in the ERA-Interim dataset). This indicates that the active basal melting can not be explained solely by the local precipitation, or that the model exaggerates the fast ice basal melting. Previous fast ice studies of Fraser et al., (2012) and Massom et al. (2010) pointed out that dynamical interactions between drifting sea ice and coastal protrusions (the coastline and ice-shelf/glacier front) play a role in the initial stage of the fast ice formation. Snow ice formation is another important process to maintain the fast ice (Zhao et al., 2020). The modeled active basal melt rates of the fast ice are accomplishable if there were enough input from drifting sea ice and/or snow ice formation.

Sea ice production is a key proxy for cold and saline water mass formation along the Antarctic coastal margins (Morales Maqueda et al., 2004; Tamura et al., 2008, 2016) because brine rejection (salt input from sea ice to the ocean when sea ice is formed) is proportional to the sea ice production. The newly-formed cold and saline water mass destratifies the local water columns, eroding the warm water intrusions onto the Antarctic coastal regions. Perennial fast ice is a very effective thermal insulator due to its thickness. Therefore, we investigate the difference in sea ice production in the two cases (Fig. 16). In the NOFI case, relatively high sea ice production areas are produced along the eastern coastline in the LHB, while in the FI case, there is zero sea ice formation in the LHB region. The combination of this result and water masses flowing into the SGT cavity (Fig. 10) indicates that the existence of fast ice in the LHB dramatically reduces surface heat flux (sea ice production) and cold water mass formation, allowing the intrusion of the unmodified warm water from the shelf break onto the LHB and into the SGT cavity in the FI case.

Fast ice has effects on the ocean conditions not only in fast ice-covered regions but also in the uncovered areas. Looking at the vertical profiles of ocean temperature and density in the box area just north of the fast ice (Fig. 11; box area indicated in Fig. 6), although there is a similar seasonal cycle in the deep layer ($\sigma_0 > 27.5$ kg m^{-3}) in the NOFI and FI cases via the wind-driven Ekman dynamics (Hirano et al., 2020; Ohshima et al., 1996), the seasonal cycle of the water properties in the surface layers is different. The surface stratification in the FI case is stronger than that in the NOFI case due to a combination of the surplus freshwater fluxes and the less-modification of the surface water by the negligible sea ice formation in the FI case. The difference in the surface stratification has an impact on the strength of undercurrent on the upper continental slope. The eastward transport of the undercurrent in the FI case is larger than that in NOFI case almost throughout the year. The stronger baroclinicity in the FI case leads to the larger eastward transport with a magnitude of about 150 mSv (approximately 50% of the annual mean transport in the NOFI case).

https://doi.org/10.5194/tc-2020-240
Preprint. Discussion started: 27 August 2020

5 Interannual variability in the model

In the model, there is substantial interannual variability in the ocean conditions in LHB and the SGT basal melting (Figs. 4 and 5). In this section, we examine the interannual variability and explore the physical links among the oceanic variables and the SGT basal melting in the model. However, it should be noted that our analysis period is too short (11 years from 2008 to 2018) to examine very-low-frequency variations (e.g., decadal variability). Furthermore, there are no observation to validate the simulated interannual variability. A comparison with the result from the CKDRF case allows us to confirm that the interannual variability in the NOFI and FI cases is not due to the model's drift or inherent variability and that the interannual-varying surface forcing causes this variability. Although the magnitudes of the basal melt rate in the NOFI and FI cases are different, the temporal evolutions of the interannual variability of the basal melting are similar to each other (Fig. 4). The interannual variability of the SGT basal melting is the largest in summer, with the standard deviation of up to 3 m yr^{-1} (Fig. 5).

As shown in Section 3, the warm water intrusions from the shelf break cause the active basal melting at SGT. Here, we show that the interannual variability of the ocean temperature in the depression (at the box) explains the temporal variability in the SGT's basal melt rate. Since the seasonal amplitudes in the ocean temperature and the SGT basal melting are larger than the interannual variability (Figs. 5 and 11), we calculated anomaly time series of the variables from the monthly climatology to examine the temporal variations in detail. The monthly climatology is the monthly mean of the variables averaged over the period 2008-2018. The upper panels in Fig. 17 show the vertical profile of the ocean temperature anomaly and density in the NOFI and FI cases. There are distinct differences in the depth range from 200 m to 600 m. We vertically averaged the temperature anomalies within this depth range to extract the temporal change in the subsurface temperature (solid lines in Fig. 17c). The time series of the subsurface temperature anomaly has a statistically significant positive correlation with those of the SGT basal melt rate. The correlation coefficients between them are r=0.63 and r=0.86 in the NOFI and FI cases, respectively. The values are above the 99% significant level (of r=0.224). The results strongly indicate that the interannual variability of the warm water in LHB is responsible for that in the SGT basal melting.

Looking at the time series of the vertically-averaged ocean temperature and the SGT basal melting anomalies (Fig. 17c), these anomalies fluctuate around zero in the period from 2008 to the first half of 2012. After that, the negative anomalies persist in the period from the second half of 2012 to the end of 2014. Subsequently, the ocean temperature and basal melting anomalies are swung to positive phases in the following period from 2015 to 2018. The vertical displacement of ocean density surfaces, which is controlled by the alongshore wind variability through Ekman dynamics (Hirano et al., 2020; Ohshima et al., 1996), partially accounts for the time series of the ocean temperature anomaly: for example, the pronounced depression of the density surfaces in 2014 is corresponding to the negative temperature anomaly. This indicates that cold surface water (i.e., WW) is depressed to deep layers, resulting in the temperature reduction in the intermediate depths.

However, the positive (warm) anomalies in the period 2015-2016 do not seem to be explained by changes in the density surfaces. We consider that changes in the ocean flow over the upper continental slope are likely responsible for the ocean temperature variability in LHB through the inflow across the sill section. Here, we utilized the strength of the eastward undercurrent on the upper continental slope as a proxy of the ocean variation outside of the bay. In the same manner for the ocean temperature and SGT basal melting, we calculated the anomaly time series of the eastward transport of the undercurrent (Fig. 14b) and compared it with the ocean temperature anomaly. The interannual variability of undercurrent transport is as large as the seasonal cycle. In the period 2015-2016, the undercurrent transport anomaly is in a pronounced positive phase, indicating the larger eastward volume transport anomaly. As shown in Fig. 12, the undercurrent on the continental slope directly links to the warm water inflow toward LHB, and the undercurrent variability is also a candidate to

https://doi.org/10.5194/tc-2020-240
Preprint. Discussion started: 27 August 2020

explain the time series of the ocean temperature anomaly. In fact, the correlation coefficients between the ocean temperature and the undercurrent transport anomalies are significantly positive (r=0.43 in the NOFI case and r=0.37 in the FI case). In summary, the ocean temperature anomaly at intermediate depths in LHB is controlled by a combination of the wind-driven local perturbation of density surfaces and the ocean flow variability on the upper continental shelf, giving rise to variability in the SGT basal melting.

6 Summary and Discussion

We have carried out numerical experiments with a high-resolution ocean-sea ice-ice shelf model to perform a detailed investigation of the ocean conditions in LHB and the basal melting at SGT. In our numerical modeling, we utilized the newly-refined local bathymetry in LHB, which includes multi-beam surveys from the JARE expeditions and depth information at control points from the Japan Coast Guard (Figs. 1 and 2). Our findings can be summarized schematically in Fig. 18. Our model can realistically capture the observed two-layer structure in LHB, consisting of cold-fresh water in the surface layer and warm-saline water in the deep layer (Fig. 7). The warm water in the deep layer is originated from the Circumpolar Deep Water on the continental slope regions. It intrudes from the submarine canyons at the shelf breaks (Figs. 6 and 9), extending southward to the SGT cavity along the eastern flank of the north-southward running deep trough (Fig. 8). The warm water intrusions are persistent throughout the year, reaching the maximum in summer and the minimum in autumn and winter. The persistent warm water intrusions into the LHB region cause active basal melting at SGT (Figs. 4, 5, and 10). The annual mean melt rates of SGT were estimated to be in a range from 8.8 m yr^{-1} (in the NOFI case) to 15.2 m yr^{-1} (in the FI case), which are much higher than the satellite-derived estimates of the circumpolar-averaged basal melt rates (Depoorter et al., 2013; Rignot et al., 2013). The predominant easterly wind in the coastal region (Fig. 3) controls the thicknesses of the cold surface and the warm deep waters (Fig. 11), and the changes in the magnitude of the warm water intrusion regulate both the seasonal and interannual variability of the SGT basal melting (Figs. 10, 11, and 17). The modeled seasonal cycle of the SGT basal melting is consistent with the seasonality of the SGT basal melting derived from the direct oceanographic and ice-radar observations (Fig. 5 and Hirano et al., 2020).

The model results showed the large seasonality of the subsurface currents under strong westward surface flows over the continental slope regions, i.e., the appearance of the eastward undercurrent in summer (Figs. 12, 13, and 14). The subsurface flows play a role in the warm water mass inflow through the submarine canyons on the sills to LHB (Fig. 12). We consider that this modeled flow pattern is a part of the Antarctic Slope Front (ASF)-Antarctic Slope Current (ASC)-Antarctic Slope Undercurrent system (Thompson et al., 2018) in this region. The ASF is a ubiquitous frontal structure formed by the prevailing easterly winds in the Antarctic coastal regions (Fig. 3), and the ASC is the corresponding strong westward-flowing ocean jet formed over the continental slope. The Antarctic Slope Undercurrent is established on the seafloor in the summer season in some Antarctic continental slope regions, satisfying the thermal wind relationship. The magnitude of the eastward-flowing undercurrent off the LHB region is greatest in the summer months (Fig. 14a) when the easterly coastal winds are at their weakest (Fig. 3i). In fact, the Antarctic Slope Undercurrent had been observed in the eastern Weddell Sea (Chavanne et al., 2010; Heywood et al., 1998; Núñez-Riboni and Fahrbach, 2009), in the Amundsen Sea (Walker et al., 2013), and in East Antarctica (Peña-Molino et al., 2016). These observational studies and the several modeling studies have pointed out that the seasonal and interannual changes of the Antarctic Slope Undercurrent play a pivotal role in water mass exchanges across the shelf breaks (Assmann et al., 2013; Silvano et al., 2019; Smedsrud et al., 2006). Until now, no observations have been made for the ocean current over the continental slope off the LHB region. If there is a seasonal undercurrent on the slope, LHB has a similar configuration to the Amundsen Sea, which has been well studied for ocean-ice

https://doi.org/10.5194/tc-2020-240
Preprint. Discussion started: 27 August 2020

shelf interaction. Since JARE performs observations within the LHB every year, LHB would be a useful monitoring site for ocean-ice shelf interaction in the East Antarctic region, although the total melting amount of the ice shelf/glacier is smaller than those of the ice shelves in the Amundsen Sea.

The existence of the multi-year fast ice characterizes LHB. The southern part of the LHB region is usually covered with a few-meters thick fast ice. We have examined the effects of the fast ice cover on the oceanic and sea ice fields and ice shelf/glacier melting, based on numerical experiments with and without the fast ice. In both experiments, the fluctuations in the alongshore wind are the main driving force for the seasonal-to-interannual variation of oceanic fields in LHB. It is found that fast ice plays a role as an insulator between the atmosphere and the ocean and suppresses local sea-ice production and cold water mass formation in the bay (Figs. 15 and 16). As a result, in the FI case, the intermediate-depth warm water intrusions from the shelf break regions reach the SGT cavity with little or no modification, resulting in higher basal melting at SGT. These modeling results strongly suggest that along with the alongshore wind, fast ice in the LHB region is an essential factor controlling the ocean-ice shelf/glacier interaction, findings reported in the other regions of East Antarctica (e.g., Fraser et al., 2019; Massom et al., 2001). In this study, we assumed the shape of the fast ice unchanged in the experiments, however, in reality, there is interannual variation in the fast ice shape and extent (Fraser et al., 2012, 2020). Therefore, it should be kept in mind that the interannual variability in the fast ice extent is also a responsible factor for those in the ocean conditions in LHB and the SGT basal melting.

Although our study area, LHB, covers only a small portion of the Antarctic coastal regions, we have been able to perform integrated research, combining topographic surveys, ship-based oceanographic observation, satellite observation, and a regionally-high resolution ocean-sea ice-ice shelf modeling. There are still large uncertainties in the bottom topography in the Antarctic coastal regions (especially thick ice-covered areas: e.g., under the fast ice and ice shelf/glacier), and the uncertainty directly links to the reliability of the numerical model results. Needless to say, further exploration of the Antarctic coastal bathymetry is required because the detailed bathymetry such as submarine canyons play a key role in the Antarctic coastal water masses and the subsequent ice-ocean interaction. We demonstrate that the high-resolution ocean modeling with the updated bottom topography can reasonably reproduce the observed oceanic field and the SGT basal melting, and such numerical modeling is useful to fill the spatiotemporal gaps in the observations. Combined with the in-situ and satellite observations, numerical modeling is a very powerful tool for a better understanding of ocean-ice shelf interaction over the Southern Ocean.

https://doi.org/10.5194/tc-2020-240
Preprint. Discussion started: 27 August 2020

Acknowledgments: KK was supported by JSPS KEKENHI Grants JP19K12301, JP17H06323. DH was supported by JSPS KEKENHI Grants JP20K12132, JP17K12811. MF was supported by JSPS KEKENHI Grants JP17H06322 and the Science Program of Japanese Antarctic Research Expedition (JARE). AF was supported by grant funding from the Australian Government as part of the Antarctic Science Collaboration Initiative program (grant ASCI000002). TT was supported by Grant-in-Aid for Scientific Research (17H04710, 17H06317 and 17H06322) from the MEXT of the Japanese Government, the Science Program of Japanese Antarctic Research Expedition (JARE) as Prioritized Research Project (AJ0902), National Institute of Polar Research (NIPR) through Project Research KP-303, the Center for the Promotion of Integrated Sciences of SOKENDAI, and the Joint Research Program of the Institute of Low Temperature Science, Hokkaido University. We express our deep gratitude to Dr. Yoshifumi Nogi for providing the bathymetry data for scientific study in Lützow-Holm Bay. The Japan Coast Guard officially provide the bathymetric data obtained onboard the Icebreaker Shirase during the JARE, including Lützow-Holm Bay. We are grateful to Dr. Shigeru Aoki and Dr. Keith Nicholls for providing the processed ApRES data.

Author contributions: K.K led this study by conducting all the numerical experiments and analyses. All authors discussed the results and comments on the manuscript.

Data availability:

LHB bottom topography: http://dx.doi.org/10.17632/z6w4xd6s3s.1#file-845c7d35-fb34-435f-bfc8-57313b60ccbf

ETOPO1: https://www.ngdc.noaa.gov/mgg/global/global.html

ETOPO5: https://www.ngdc.noaa.gov/mgg/global/etopo5.HTML

GEBCO: https://www.gebco.net/data_and_products/historical_data_sets/#gebco_one

RTopo1: https://doi.pangaea.de/10.1594/PANGAEA.741917.

Rtopo2: https://doi.pangaea.de/10.1594/PANGAEA.856844

PHC: http://psc.apl.washington.edu/nonwp_projects/PHC/Climatology.html.

ERA-Interim: http://www.ecmwf.int/en/research/climate-reanalysis/era-interim.

All numerical experiments were conducted using COCO (https://ccsr.aori.u-tokyo.ac.jp/~hasumi/COCO/) with an ice-shelf component (Kusahara and Hasumi, 2013) and all the numerical model results for the plots in this study will available in a data repository with a reserved doi (http://dx.doi.org/10.17632/z6w4xd6s3s.1).

Competing interest: The authors declare no conflict of interest.

https://doi.org/10.5194/tc-2020-240
Preprint. Discussion started: 27 August 2020

References

Adcroft, A., Hill, C. and Marshall, J.: Representation of Topography by Shaved Cells in a Height Coordinate Ocean Model, Mon. Weather Rev., 125(9), 2293–2315, doi:10.1175/1520-0493(1997)125<2293:rotbsc>2.0.co;2, 2002.

Amante, C. and Eakins, B. W.: ETOPO1 1 Arc-Minute Global Relief Model: Procedures, Data Sources and Analysis., 2009.

Aoki, S.: Breakup of land-fast sea ice in Lützow-Holm Bay, East Antarctica, and its teleconnection to tropical Pacific sea surface temperatures, Geophys. Res. Lett., 44(7), 3219–3227, doi:10.1002/2017GL072835, 2017.

Assmann, K. M., Jenkins, A., Shoosmith, D. R., Walker, D. P., Jacobs, S. S. and Nicholls, K. W.: Variability of circumpolar deep water transport onto the Amundsen Sea Continental shelf through a shelf break trough, J. Geophys. Res. Ocean., 118(12), 6603–6620, doi:10.1002/2013JC008871, 2013.

Bitz, C. M. and Lipscomb, W. H.: An energy-conserving thermodynamic model of sea ice, J. Geophys. Res., 104(C7), 15669–15677, doi:10.1029/1999JC900100, 1999.

Chavanne, C. P., Heywood, K. J., Nicholls, K. W. and Fer, I.: Observations of the Antarctic Slope undercurrent in the Southeastern Weddell Sea, Geophys. Res. Lett., 37(13), doi:10.1029/2010GL043603, 2010.

Conkright, M., Levitus, S., O'Brien, T., Boyer, T. P., Stephens, C., Johnson, D., Baranova, O., Antonov, J., R. Gelfeld, J., Rochester and Forgy, C.: World Ocean Database 1998: Documentation and quality control version 2.0, Natl. Oceanogr. Data Cent. Intern. Report, Silver Spring, MD, 14, 127 pp [online] Available from: http://scholar.google.com/scholar?hl=en&btnG=Search&q=intitle:WORLD+OCEAN+DATABASE+1998+Documentation+and+Quality+Control#1, 1999.

Convey, P., Bindschadler, R., di Prisco, G., Fahrbach, E., Gutt, J., Hodgson, D. A., Mayewski, P. A., Summerhayes, C. P. and Turner, J.: Antarctic climate change and the environment, Antarct. Sci., 21(06), 541, doi:10.1017/s0954102009990642, 2009.

Dee, D. P., Uppala, S. M., Simmons, A. J., Berrisford, P., Poli, P., Kobayashi, S., Andrae, U., Balmaseda, M. a., Balsamo, G., Bauer, P., Bechtold, P., Beljaars, a. C. M., van de Berg, L., Bidlot, J., Bormann, N., Delsol, C., Dragani, R., Fuentes, M., Geer, a. J., Haimberger, L., Healy, S. B., Hersbach, H., Hólm, E. V., Isaksen, L., Kållberg, P., Köhler, M., Matricardi, M., Mcnally, a. P., Monge-Sanz, B. M., Morcrette, J. J., Park, B. K., Peubey, C., de Rosnay, P., Tavolato, C., Thépaut, J. N. and Vitart, F.: The ERA-Interim reanalysis: Configuration and performance of the data assimilation system, Q. J. R. Meteorol. Soc., 137(656), 553–597, doi:10.1002/qj.828, 2011.

Depoorter, M. A., Bamber, J. L., Griggs, J. A., Lenaerts, J. T. M., Ligtenberg, S. R. M., van den Broeke, M. R. and Moholdt, G.: Calving fluxes and basal melt rates of Antarctic ice shelves., Nature, 502(7469), 89–92, doi:10.1038/nature12567, 2013.

Fraser, A. D., Massom, R. A., Michael, K. J., Galton-Fenzi, B. K. and Lieser, J. L.: East antarctic landfast sea ice distribution and variability, 2000-08, J. Clim., 25(4), 1137–1156, doi:10.1175/JCLI-D-10-05032.1, 2012.

Fraser, A. D., Ohshima, K. I., Nihashi, S., Massom, R. A., Tamura, T., Nakata, K., Williams, G. D., Carpentier, S. and Willmes, S.: Landfast ice controls on sea-ice production in the Cape Darnley Polynya: A case study, Remote Sens. Environ., 233, doi:10.1016/j.rse.2019.111315, 2019.

Fraser, A. D., Massom, R. A., Ohshima, K. I., Willmes, S., Kappes, P. J., Cartwright, J. and Porter-Smith, R.: High-resolution mapping of circum-Antarctic landfast sea ice distribution, 2000–2018, Earth Syst. Sci. Data Discuss., doi:10.5194/essd-2020-99, 2020.

Giles, A. B., Massom, R. A. and Lytle, V. I.: Fast-ice distribution in East Antarctica during 1997 and 1999 determined using RADARSAT data, J. Geophys. Res., 113(C2), C02S14, doi:10.1029/2007JC004139, 2008.

Gille, S. T., McKee, D. C. and Martinson, D. G.: Temporal changes in the Antarctic circumpolar current: Implications for the Antarctic continental shelves, Oceanography, 29(4), 96–105, doi:10.5670/oceanog.2016.102, 2016.

Gordon, A. L.: Current Systems in the Southern Ocean, Encycl. Ocean Sci. Second Ed., 735–743, doi:10.1016/B978-012374473-9.00369-6, 2008.

Gwyther, D. E., Kusahara, K., Asay-Davis, X. S., Dinniman, M. S. and Galton-Fenzi, B. K.: Vertical processes and resolution impact ice shelf basal melting: A multi-model study, Ocean Model., 147, doi:10.1016/j.ocemod.2020.101569, 2020.

Hellmer, H. H. and Olbers, D. J.: A two-dimensional model for the thermohaline circulation under an ice shelf, Antarct. Sci., 1(4), 325–336, doi:10.1017/S0954102089000490, 1989.

Heywood, K. J., Locarnini, R. A., Frew, R. D., Dennis, P. F. and King, B. A.: Transport and Water Masses of the Antarctic Slope Front System in The Eastern Weddell Sea, pp. 203–214., 1998.

Hibler, W. D.: A dynamic thermodynamic sea ice model, J. Phys. Oceanogr., 9(4), 815–846, doi:10.1175/1520-0485(1979)009<0815:ADTSIM>2.0.CO;2, 1979.

Hirano, D., Tamura, T., Kusahara, K., Ohshima, K. I., Nicholls, K. W., Ushio, S., Simizu, D., Ono, K., Fujii, M., Nogi, Y. and Aoki, S.: Strong ice-ocean interaction beneath Shirase Glacier Tongue in East Antarctica, Nat. Commun., 11(1), 4221, doi:10.1038/s41467-020-17527-4, 2020.

Holland, D. M. and Jenkins, A.: Modeling thermodynamic ice–ocean interactions at the base of an ice shelf, J. Phys. Oceanogr., 29(8), 1787–1800, doi:10.1175/1520-0485(1999)029<1787:MTIOIA>2.0.CO;2, 1999.

Hunke, E. C. and Dukowicz, J. K.: An elastic-viscous-plastic model for sea ice dynamics, J. Phys. Oceanogr., 27(9), 1849–1867, doi:10.1175/1520-0485(1997)027<1849:AEVPMF>2.0.CO;2, 1997.

IOC, IHO and BODC: GEBCO digital atlas, 2003.

Jacobs, S. S., Hellmer, H. H. and Jenkins, A.: Antarctic Ice Sheet melting in the southeast Pacific, Geophys. Res. Lett., 23(9), 957, doi:10.1029/96GL00723, 1996.

Jenkins, A., Shoosmith, D., Dutrieux, P., Jacobs, S., Kim, T. W., Lee, S. H., Ha, H. K. and Stammerjohn, S.: West Antarctic Ice Sheet retreat in the Amundsen Sea driven by decadal oceanic variability, Nat. Geosci., doi:10.1038/s41561-018-0207-4, 2018.

Kara, A. B., Rochford, P. A. and Hurlburt, H. E.: Efficient and accurate bulk parameterizations of air–sea fluxes for use in general circulation models, J. Atmos. Ocean. Technol., 17(10), 1421–1438, doi:10.1175/1520-0426(2000)017<1421:EAABPO>2.0.CO;2, 2000.

Kusahara, K. and Hasumi, H.: Modeling Antarctic ice shelf responses to future climate changes and impacts on the ocean, J. Geophys. Res. Ocean., 118(5), 2454–2475, doi:10.1002/jgrc.20166, 2013.

Kusahara, K. and Hasumi, H.: Pathways of basal meltwater from Antarctic ice shelves: A model study, J. Geophys. Res. Ocean., 119(9), 5690–5704, doi:10.1002/2014JC009915, 2014.

Kusahara, K., Hasumi, H. and Tamura, T.: Modeling sea ice production and dense shelf water formation in coastal polynyas around East Antarctica, J. Geophys. Res. Ocean., 115(10), doi:10.1029/2010JC006133, 2010.

Kusahara, K., Williams, G. D., Tamura, T., Massom, R. and Hasumi, H.: Dense Shelf Water spreading from Antarctic coastal polynyas to the deep Southern Ocean: A regional circumpolar model study, J. Geophys. Res. Ocean., doi:10.1002/2017JC012911, 2017.

Losch, M.: Modeling ice shelf cavities in a z coordinate ocean general circulation model, J. Geophys. Res., 113, C08043, doi:10.1029/2007JC004368, 2008.

Marsland, S. J., Bindoff, N. L., Williams, G. D. and Budd, W. F.: Modeling water mass formation in the Mertz Glacier Polynya and Adélie Depression, East Antarctica, J. Geophys. Res., 109(C11), C11003, doi:10.1029/2004JC002441, 2004.

Marsland, S. J., Church, J. A., Bindoff, N. L. and Williams, G. D.: Antarctic coastal polynya response to climate change, J. Geophys. Res. Ocean., 112(7), C07009, doi:10.1029/2005JC003291, 2007.

Massom, R. A., Hill, K. L., Lytle, V. I., Worby, A. P., Paget, M. J. and Allison, I.: Effects of regional fast-ice and iceberg distributions on the behaviour of the Mertz Glacier polynya, East Antarctica, Ann. Glaciol., 33, 391–398, doi:10.3189/172756401781818518, 2001.

https://doi.org/10.5194/tc-2020-240
Preprint. Discussion started: 27 August 2020

Massom, R. A., Giles, B., Fricker, H. A., Warner, R. C., Legrésy, B., Hyland, G., Young, N. and Fraser, A. D.: Examining the interaction between multi-year landfast sea ice and the Mertz Glacier Tongue, East Antarctica: Another factor in ice sheet stability?, J. Geophys. Res. Ocean., 115(12), 1–15, doi:10.1029/2009JC006083, 2010.

Mellor, G. L. and Kantha, L.: An ice-ocean coupled model, J. Geophys. Res., 94(C8), 10,937-10,954, 1989.

Morales Maqueda, M. A., Willmott, A. J. and Biggs, N. R. T.: Polynya Dynamics: A review of observations and modeling, Rev. Geophys., 42, RG1004, doi:10.1029/2002RG000116, 2004.

Moriwaki, K. and Yoshida, Y.: Submarine topography of Lutzow Holm Bay, Antarctica., Mem. Inst. Polar Res. Tokyo, 28, 247–258, 1983.

Nakamura, K., Doi, K. and Shibuya, K.: Fluctuations in the flow velocity of the Antarctic Shirase Glacier over an 11-year period, Polar Sci., doi:10.1016/j.polar.2010.04.010, 2010.

Nihashi, S. and Ohshima, K. I.: Circumpolar mapping of Antarctic coastal polynyas and landfast sea ice: relationship and variability, J. Clim., 28(9), 3650–3670, doi:10.1175/JCLI-D-14-00369.1, 2015.

Nitsche, F. O., Porter, D., Williams, G., Cougnon, E. A., Fraser, A. D., Correia, R. and Guerrero, R.: Bathymetric control of warm ocean water access along the East Antarctic Margin, Geophys. Res. Lett., doi:10.1002/2017GL074433, 2017.

NOAA: ETOPO5 5-minute gridded elevation data, Online: http://www.ngdc.noaa.gov/mgg/global/etopo5.HTML (accessed 02/05/2012), 8641, 1988.

Núñez-Riboni, I. and Fahrbach, E.: Seasonal variability of the Antarctic Coastal Current and its driving mechanisms in the Weddell Sea, Deep. Res. Part I Oceanogr. Res. Pap., 56(11), 1927–1941, doi:10.1016/j.dsr.2009.06.005, 2009.

Ohshima, K. I.: Effect of landfast sea ice on coastal currents driven by the wind, J. Geophys. Res. Ocean., 105(C7), 17133–17141, doi:10.1029/2000jc900081, 2000.

Ohshima, K. I., Takizawa, T., Ushio, S. and Kawamura, T.: Seasonal variations of the Antarctic coastal ocean in the vicinity of Lützow-Holm Bay, J. Geophys. Res., 101(C9), 20617, doi:10.1029/96JC01752, 1996.

Paolo, F. S., Fricker, H. A. and Padman, L.: Volume loss from Antarctic ice shelves is accelerating, Science (80-.)., 348(6232), 327–331, doi:10.1126/science.aaa0940, 2015.

Peña-Molino, B., McCartney, M. S. and Rintoul, S. R.: Direct observations of the Antarctic Slope Current transport at 113°E, J. Geophys. Res. Ocean., 121(10), 7390–7407, doi:10.1002/2015JC011594, 2016.

Rignot, E.: Mass balance of East Antarctic glaciers and ice shelves from satellite data, Ann. Glaciol., 34, 217–227, doi:10.3189/172756402781817419, 2002.

Rignot, E., Velicogna, I., Van Den Broeke, M. R., Monaghan, A. and Lenaerts, J.: Acceleration of the contribution of the Greenland and Antarctic ice sheets to sea level rise, Geophys. Res. Lett., 38(5), L05503, doi:10.1029/2011GL046583, 2011.

Rignot, E., Jacobs, S., Mouginot, J. and Scheuchl, B.: Ice-shelf melting around Antarctica, Science (80-.)., 341(6143), 266–270, doi:10.1126/science.1235798, 2013.

Rignot, E., Mouginot, J., Scheuchl, B., Van Den Broeke, M., Van Wessem, M. J. and Morlighem, M.: Four decades of Antarctic ice sheet mass balance from 1979–2017, Proc. Natl. Acad. Sci. U. S. A., 116(4), 1095–1103, doi:10.1073/pnas.1812883116, 2019.

Rintoul, S. R., Silvano, A., Pena-Molino, B., van Wijk, E., Rosenberg, M., Greenbaum, J. S. and Blankenship, D. D.: Ocean heat drives rapid basal melt of the Totten Ice Shelf, Sci. Adv., doi:10.1126/sciadv.1601610, 2016.

Schaffer, J., Timmermann, R., Erik Arndt, J., Savstrup Kristensen, S., Mayer, C., Morlighem, M. and Steinhage, D.: A global, high-resolution data set of ice sheet topography, cavity geometry, and ocean bathymetry, Earth Syst. Sci. Data, 8(2), 543–557, doi:10.5194/essd-8-543-2016, 2016.

Silvano, A., Rintoul, S. and Herraiz-Borreguero, L.: Ocean-Ice Shelf Interaction in East Antarctica, Oceanography, doi:10.5670/oceanog.2016.105, 2016.

Silvano, A., Rintoul, S. R., Peña-Molino, B., Hobbs, W. R., Van Wijk, E., Aoki, S., Tamura, T. and Williams, G. D.: Freshening by glacial meltwater enhances melting of ice shelves and reduces formation of Antarctic Bottom Water, Sci. Adv., doi:10.1126/sciadv.aap9467, 2018.

Silvano, A., Rintoul, S. R., Kusahara, K., Peña-Molino, B., van Wijk, E., Gwyther, D. E. and Williams, G. D.: Seasonality of Warm Water Intrusions Onto the Continental Shelf Near the Totten Glacier, J. Geophys. Res. Ocean., doi:10.1029/2018JC014634, 2019.

Smedsrud, L. H., Jenkins, A., Holland, D. M. and Nøst, O. a.: Modeling ocean processes below Fimbulisen, Antarctica, J. Geophys. Res. Ocean., 111(1), C01107, doi:10.1029/2005JC002915, 2006.

Steele, M., Steele, M., Morley, R., Morley, R., Ermold, W. and Ermold, W.: PHC: A global ocean hydrography with a high quality Arctic Ocean, J. Clim., 14, 2079–2087, doi:10.1175/1520-0442, 2001.

Tamura, T., Ohshima, K. I. and Nihashi, S.: Mapping of sea ice production for Antarctic coastal polynyas, Geophys. Res. Lett., 35(7), doi:10.1029/2007GL032903, 2008.

Tamura, T., Ohshima, K. I., Fraser, A. D. and Williams, G. D.: Sea ice production variability in Antarctic coastal polynyas, J. Geophys. Res., 2967--2979, doi:10.1002/2015JC011486, 2016.

Thompson, A. F., Stewart, A. L., Spence, P. and Heywood, K. J.: The Antarctic Slope Current in a Changing Climate, Rev. Geophys., 56(4), 741–770, doi:10.1029/2018RG000624, 2018.

Timmermann, R., Le Brocq, A., Deen, T., Domack, E., Dutrieux, P., Galton-Fenzi, B., Hellmer, H., Humbert, A., Jansen, D., Jenkins, A., Lambrecht, A., Makinson, K., Niederjasper, F., Nitsche, F., Nøst, O. A., Smedsrud, L. H. and Smith, W. H. F.: A consistent dataset of Antarctic ice sheet topography, cavity geometry, and global bathymetry, Earth Syst. Sci. Data Discuss., 3(2), 231–257, doi:10.5194/essdd-3-231-2010, 2010.

Turner, J., Bindschadler, R.A. Convey, P., Di Prisco, G., Fahrbach, E., Gutt, J., Hodgson, D. A. and Mayewski P.A. Summerhayes, C. .: Antarctic Climate Change and the Environment., 2009.

Ushio, S.: Factors affecting fast-ice break-up frequency in Lützow-Holm Bay, Antarctica, Ann. Glaciol., 44, 177–182, doi:10.3189/172756406781811835, 2006.

Walker, D. P., Jenkins, A., Assmann, K. M., Shoosmith, D. R. and Brandon, M. A.: Oceanographic observations at the shelf break of the Amundsen Sea, Antarctica, J. Geophys. Res. Ocean., 118(6), 2906–2918, doi:10.1002/jgrc.20212, 2013.

Zhao, J., Cheng, B., Vihma, T., Heil, P., Hui, F., Shu, Q., Zhang, L. and Yang, Q.: Fast Ice Prediction System (FIPS) for land-fast sea ice at Prydz Bay, East Antarctica: an operational service for CHINARE, Ann. Glaciol., 1–13, doi:10.1017/aog.2020.46, 2020.

https://doi.org/10.5194/tc-2020-240
Preprint. Discussion started: 27 August 2020

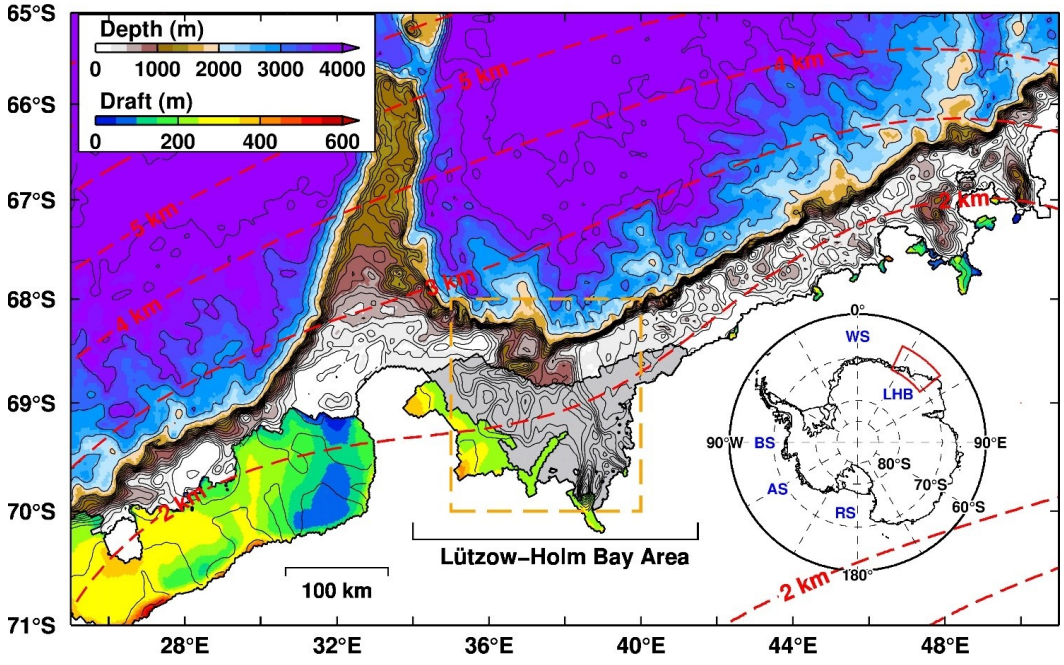

Figure 1: Bottom topography and the draft of ice shelves/glaciers around the Lützow-Holm Bay (LHB) area. Red dashed contours indicate the horizontal grid spacing in the model. Map inset shows our focal region in the Southern Ocean. Gray shaded areas are fast ice regions. Background bottom topography is derived from ETOPO1 dataset, and the local topography in the area enclosed with an orange box is replaced with the newly-compiled dataset (section 2.2 and Fig. 2a). Major place names are shown in the inset: Weddell Sea (WS), Ross Sea (RS), Amundsen Sea (AS), and Bellingshausen Sea (BS).

https://doi.org/10.5194/tc-2020-240
Preprint. Discussion started: 27 August 2020

The Cryosphere
Discussions
Open Access
EGU

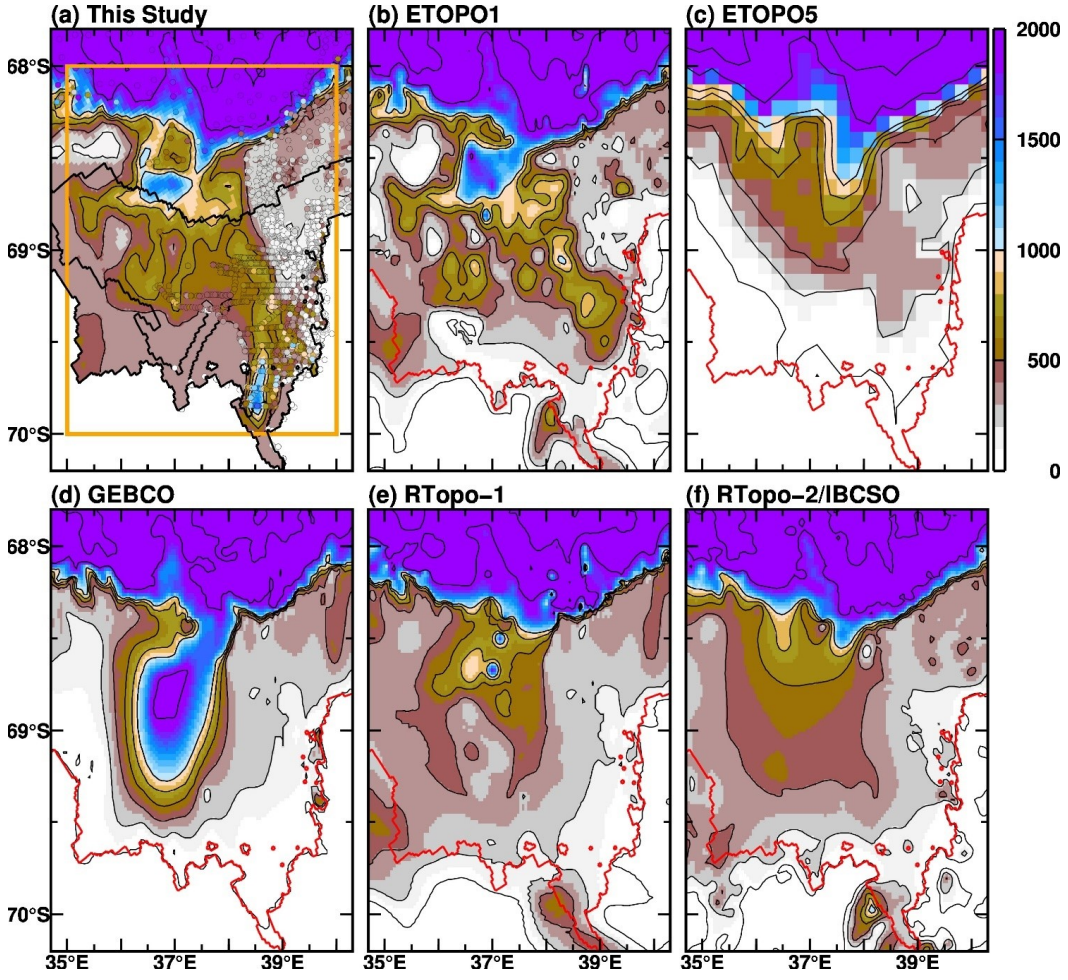

Figure 2: Comparison of water depth representation in the topographic datasets (a: this study, b: ETOPO1, c: ETOPO5, d: GEBCO, e: Rtopo-1, and f: Rtopo-2/IBCSO). The red lines in the panels b-f indicate the grounding line in the model (a). Circles with color in the panel (a) are observed depth measurements from the point echo sounding using sea ice drill holes and the JCB nautical chart (subsampled to avoid clutter in the panel).

https://doi.org/10.5194/tc-2020-240
Preprint. Discussion started: 27 August 2020

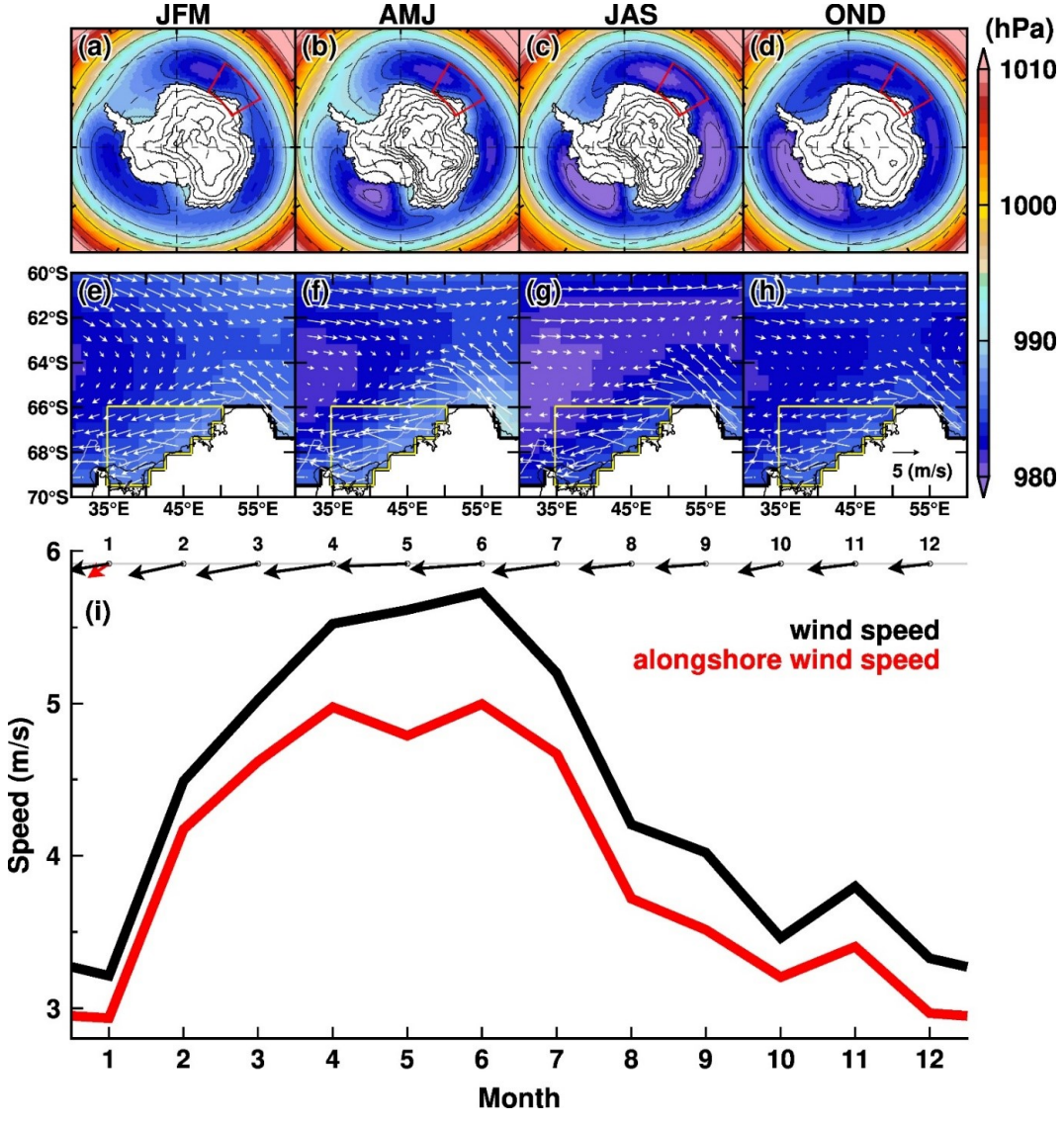

720

Figure 3: Seasonal climatology of atmospheric circulation (a-d) over the Southern Ocean and (e-f) in the region off Lützow-Holm Bay. Color and vectors show the 3-month average of surface air pressure and 10-m wind fields, respectively. The climatology is calculated from the ERA-Interim dataset for the period 1979-2018. The red box in the upper panels indicates the region for the panels (e)-(h). The area enclosed by the yellow line in the middle panels is the area for averaging the 10-m wind for the panel (i). In the panel (i), the monthly
725 climatologies of wind vector and wind speeds (black: absolute speed and red: alongshore speed) are displayed. The red vector in January is a unit vector of the defined alongshore direction.

https://doi.org/10.5194/tc-2020-240
Preprint. Discussion started: 27 August 2020

The Cryosphere Discussions
Open Access
EGU

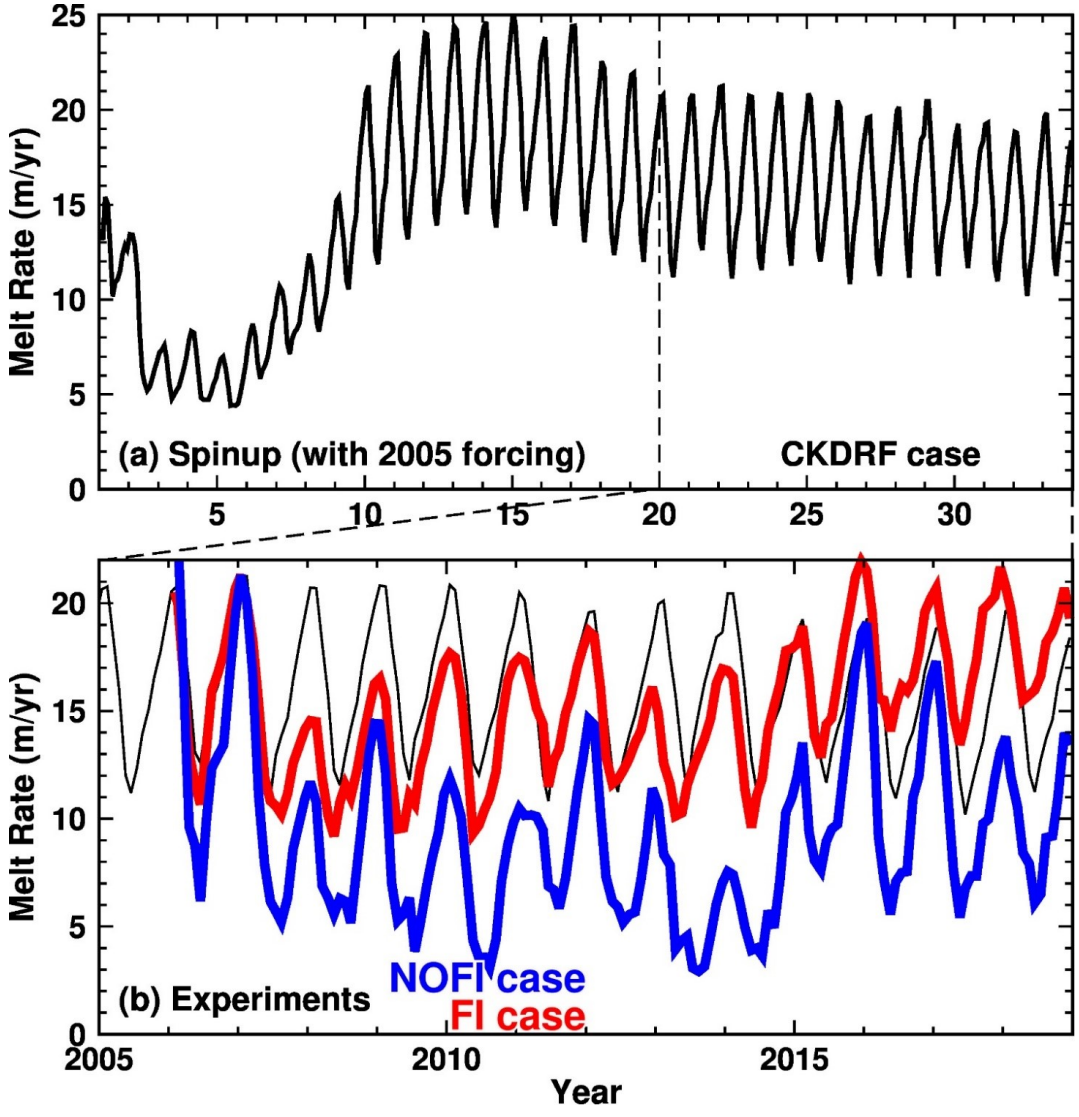

Figure 4: Time series of basal melt rate at Shirase Glacier Tongue (a: the full integration period of 33 years including periods of the initial 20-year spin-up and the CKDRF case, b: the last 14 years corresponding to the period 2005-2018). In panel (b), blue, red, and black lines show the results from the NOFI, FI, and CKDRF cases, respectively. The equivalent annual melt rate (m yr^{-1}) is used for the vertical scale.

https://doi.org/10.5194/tc-2020-240
Preprint. Discussion started: 27 August 2020

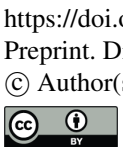

The Cryosphere
Discussions
Open Access
EGU

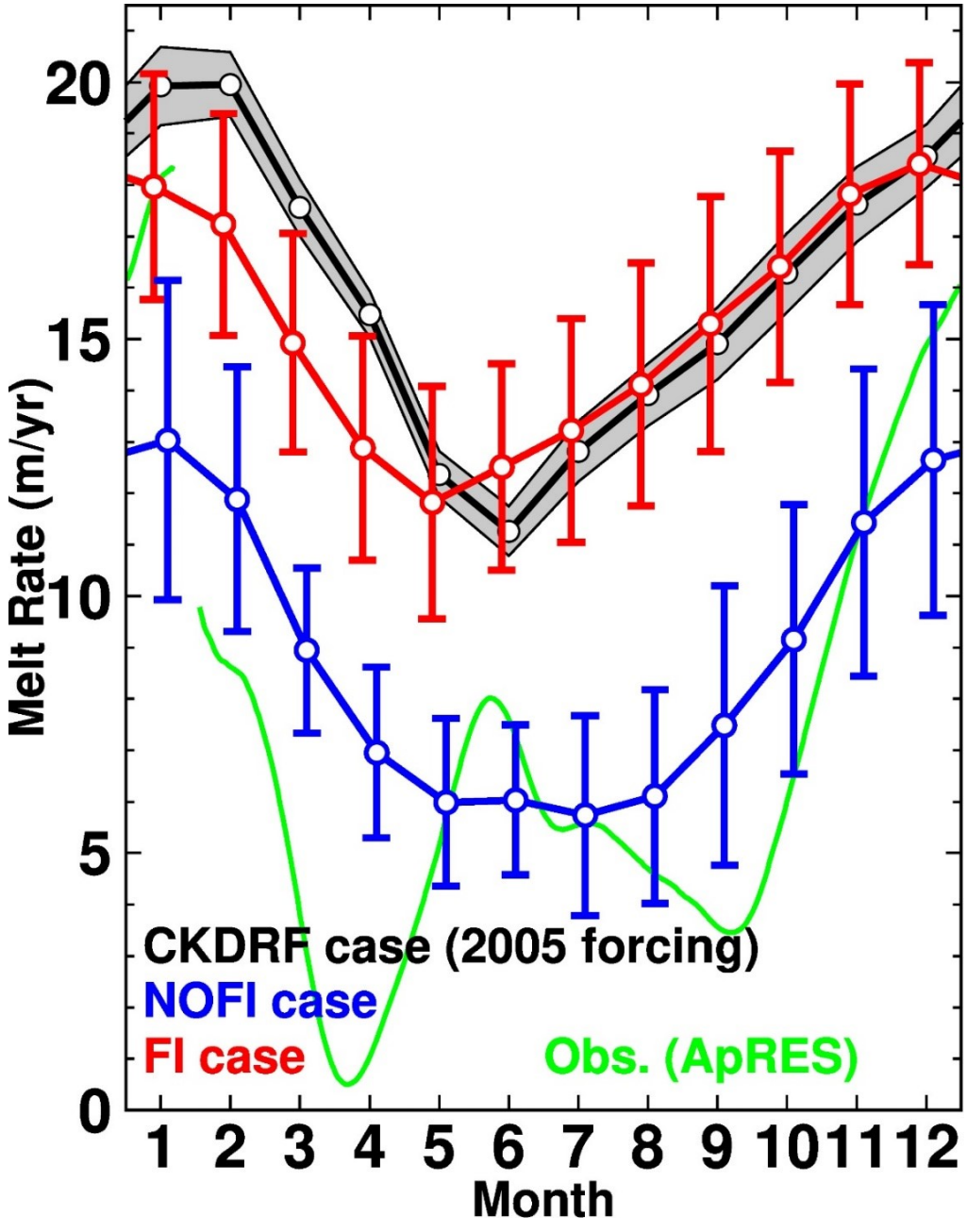

Figure 5: Seasonal variation of basal melt rate at Shirase Glacier Tongue. Black, blue, red, and green lines show results from the CKDRF, NOFI, FI cases, and ice radar-derived estimate (ApRES, Hirano et. al. 2020), respectively. Shade or vertical bars indicate the standard deviation of the monthly basal melt rate in the period 2008-2018, showing the model's inherent variability and interannual variability. The scale of the vertical axis is the equivalent annual melt rate (m yr^{-1}).

https://doi.org/10.5194/tc-2020-240
Preprint. Discussion started: 27 August 2020

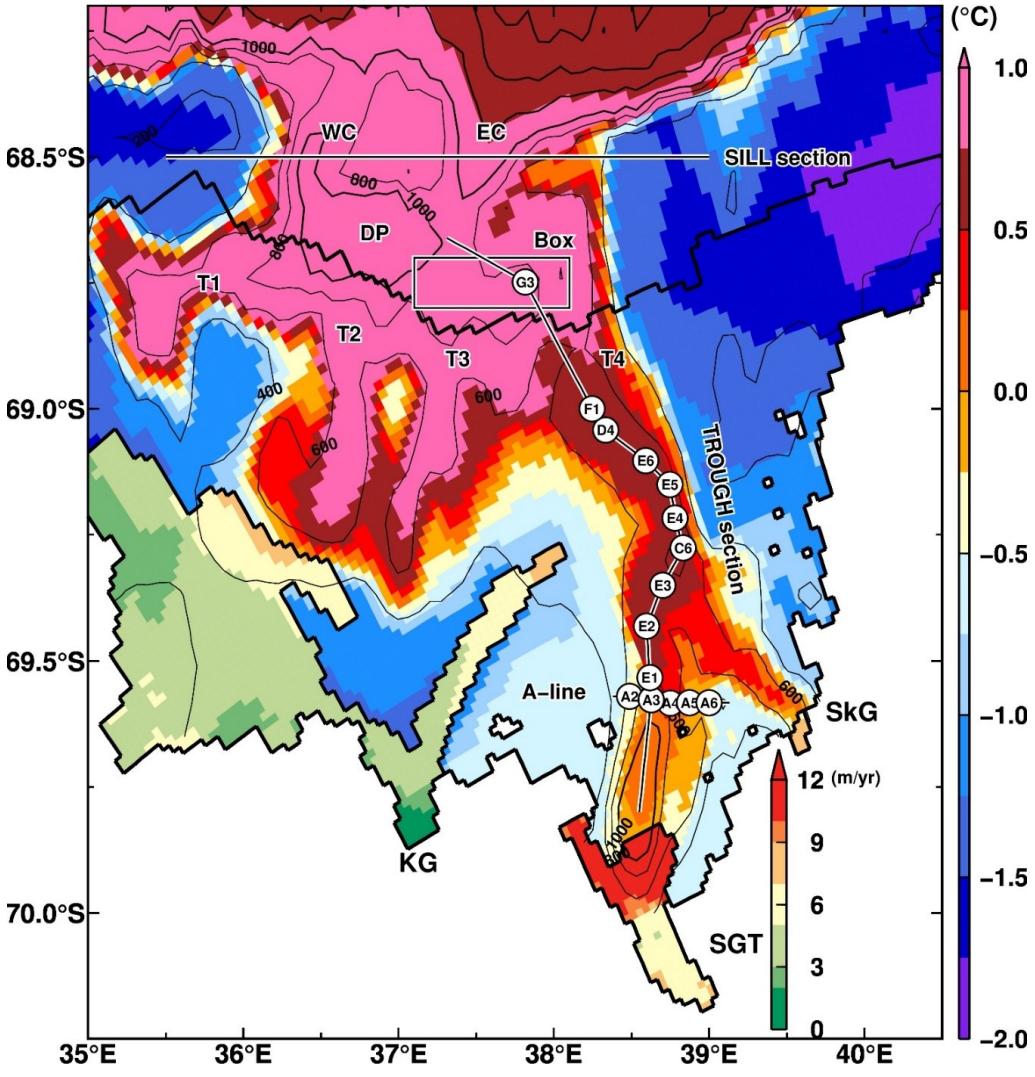

Figure 6: Map of the modeled ocean bottom temperature in January and annual mean basal melt rate in the NOFI case. The variables were averaged over the period 2008-2018. White circles with station names show positions of the in-situ oceanographic observations for the comparisons in Figs. 7 and 8. Black lines connecting the observational stations are defined as TROUGH section and A-line. SGT indicates the Shirase Glacier Tongue, SkG the Skallen Glacier, KG the Kaya Glacier. WC and EC are placed to refer to the western and eastern submarine canyons, respectively. T1, T2, T3, T4 are placed to refer to the troughs in the LHB. Sill sections near the shelf break are used to show vertical profiles in Fig 9. A box is used for averaging ocean properties in Figs. 11 and 17.

https://doi.org/10.5194/tc-2020-240
Preprint. Discussion started: 27 August 2020

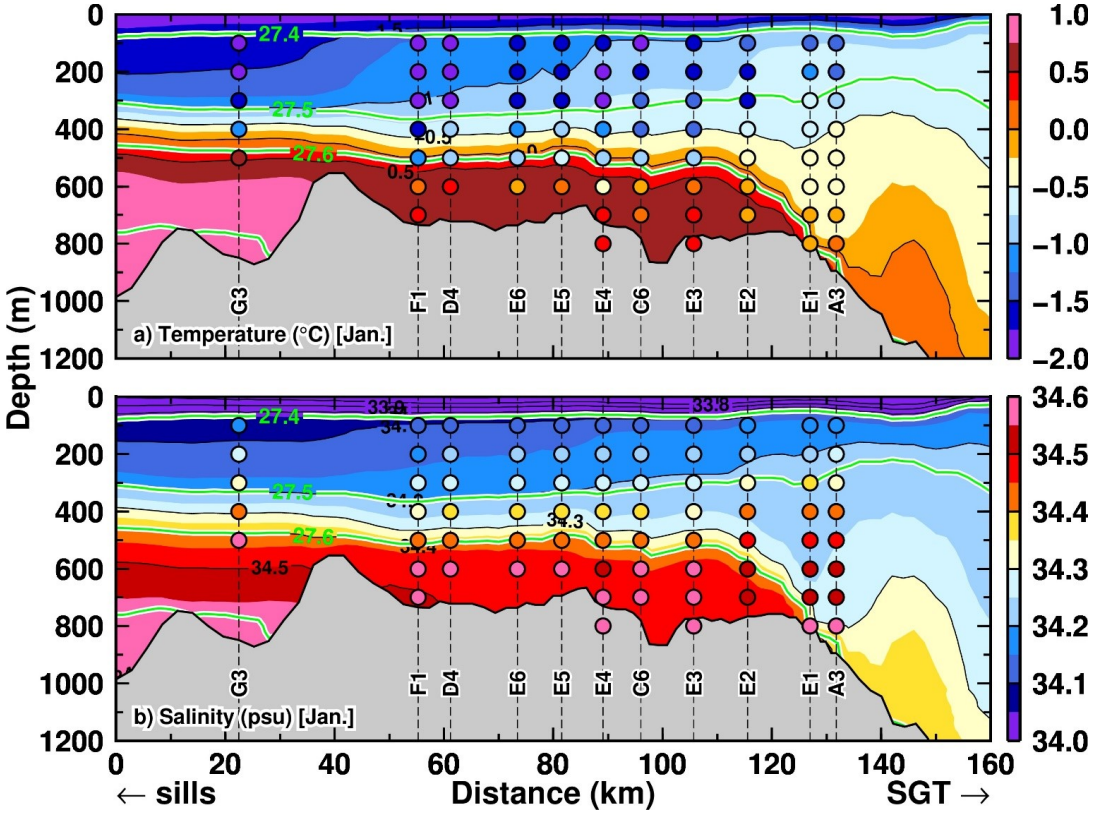

Figure 7: Vertical profiles of (a) potential temperature and (b) salinity along the TROUGH section in January in the NOFI case. Green curves indicate the contours of potential density anomalies. The model's variables were averaged over the period 2008-2018. The horizontal axis indicates the distance from the starting point of the TROUGH section located near the deepest depression in LHB (see the line of the TROUGH section in Fig. 6). Circles filled with the color at vertical dashed lines indicate the observed ocean properties in January/February 2016 (Hirano et al., 2020).

https://doi.org/10.5194/tc-2020-240
Preprint. Discussion started: 27 August 2020

The Cryosphere
Discussions
Open Access
EGU

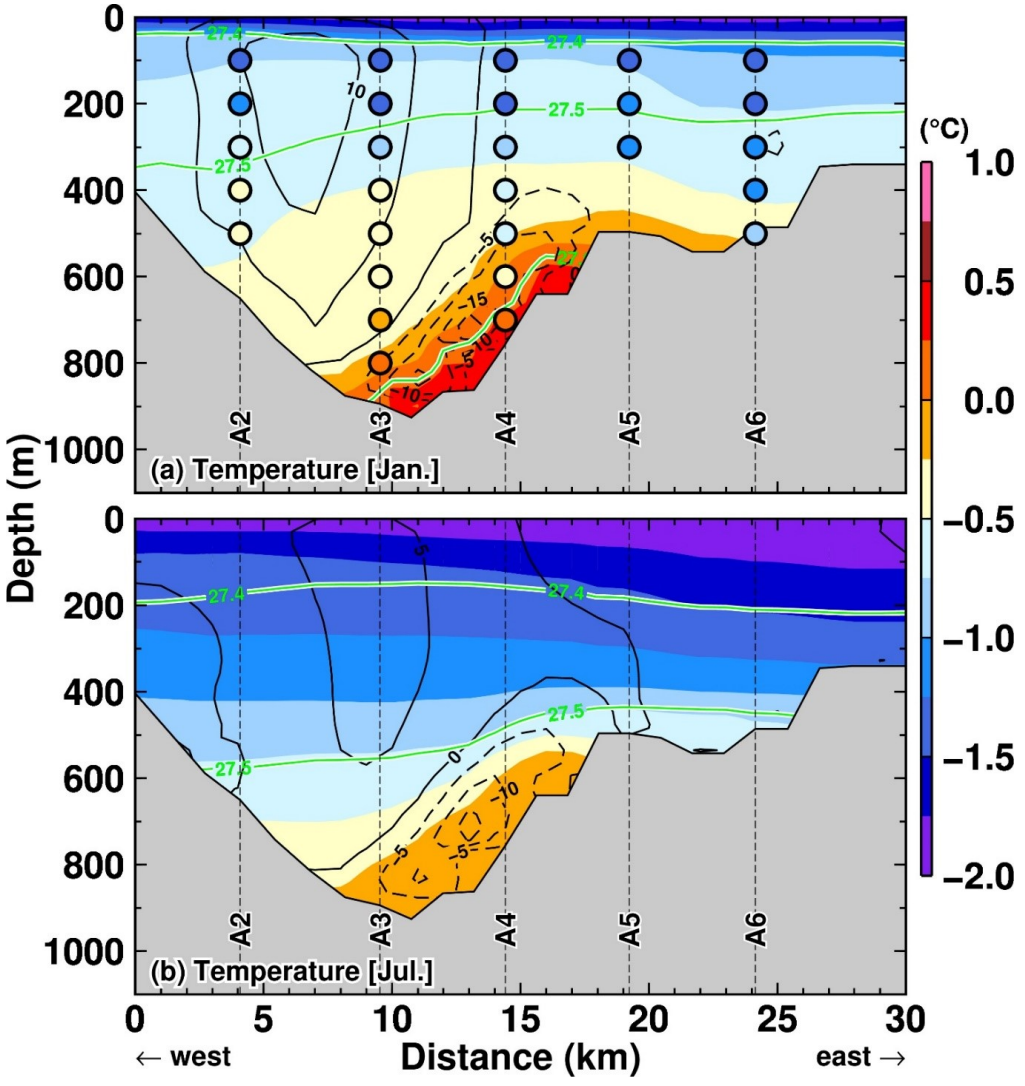

Figure 8: Vertical profiles of potential temperature along the A-line in (a) January and (b) July in the NOFI case, with the velocity normal to the section (cm s^{-1}). Positive velocity indicates northward flow. Green curves indicate contours of potential density anomalies. The model's variables were averaged over the period 2008-2018. The horizontal axis indicates the distance from the starting point of the A-line section (see the line of the A-line in Fig. 6). Circles filled with the color in the panel a indicates the observed ocean properties in January/February 2016 (Hirano et al., 2020).

https://doi.org/10.5194/tc-2020-240
Preprint. Discussion started: 27 August 2020

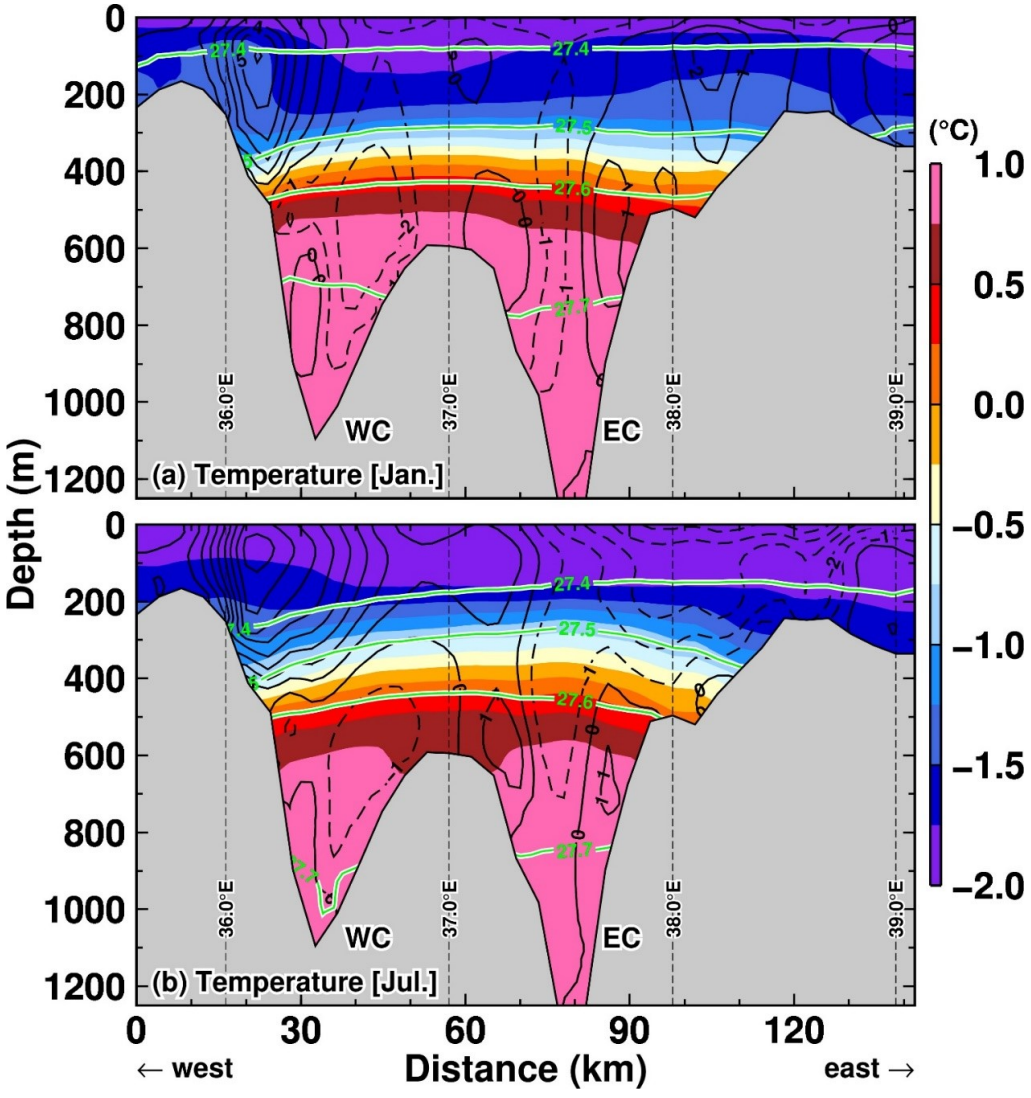

760 **Figure 9:** Vertical profiles of potential temperature along the sill section (at 68.5°S) in (a) January and (b) July in the NOFI case, with the velocity normal to the section (cm s^{-1}). Positive velocity indicates northward flow. Green curves indicate the contours of potential density anomalies. The model's variables were averaged over the period 2008-2018. The horizontal axis indicates the distance from the western side starting point of the sill section (see the line of the sill section in Fig. 6).

765

https://doi.org/10.5194/tc-2020-240
Preprint. Discussion started: 27 August 2020

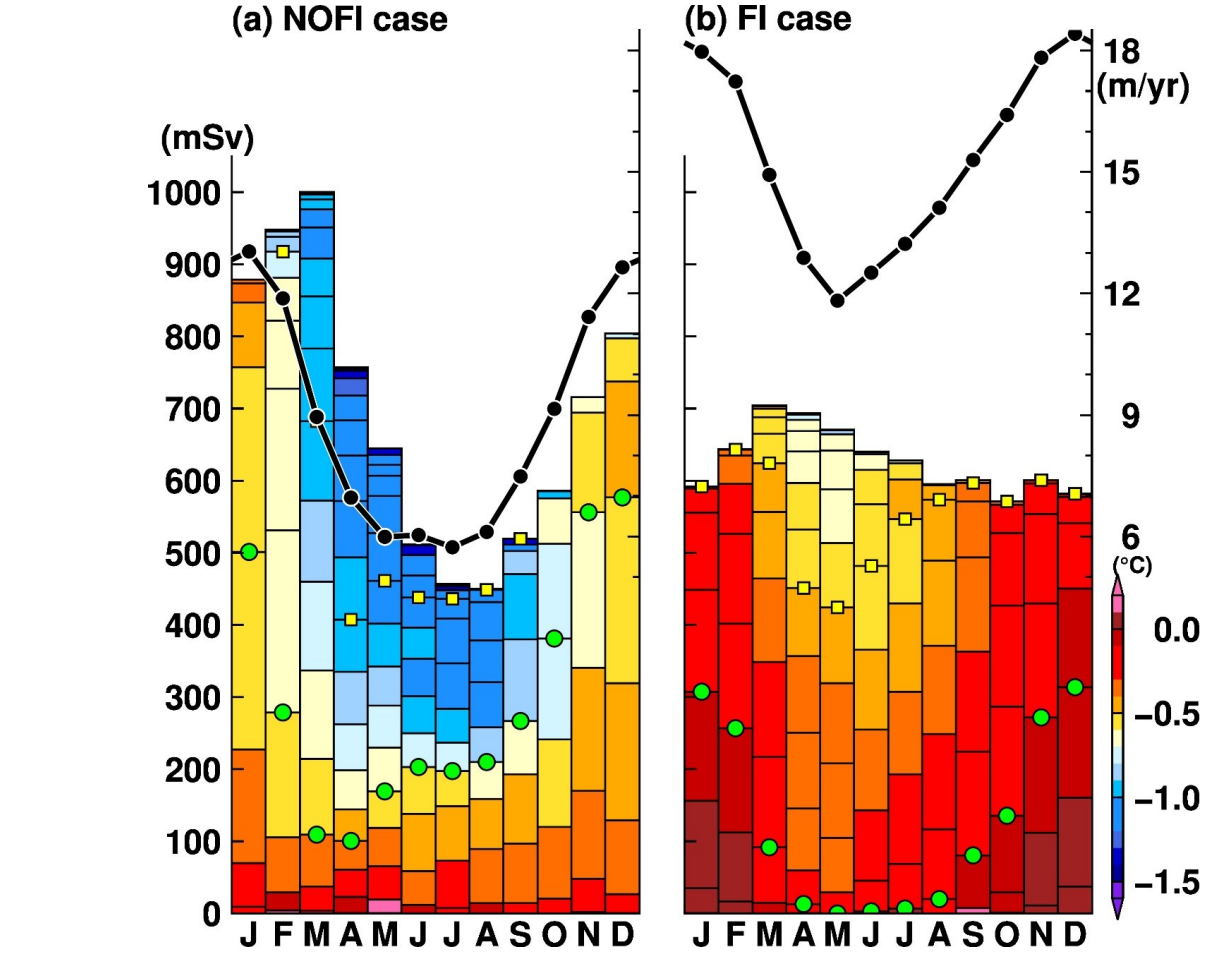

Figure 10: Seasonal variation of water mass transport flowing into the SGT cavity (mSv, left axis) with the potential temperature in potential density anomaly bin with 0.02 kg m^{-3} (color) and the mean basal melt rate (m yr^{-1}, right axis) in the (a) NOFI and (b) CTRL cases. Green dots and yellow squares represent boundaries of 27.5 and 27.4 kg m^{-3} of the potential density anomaly, respectively. The variables were averaged over the period 2008-2018.

https://doi.org/10.5194/tc-2020-240
Preprint. Discussion started: 27 August 2020

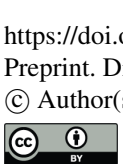

The Cryosphere
Discussions
Open Access
EGU

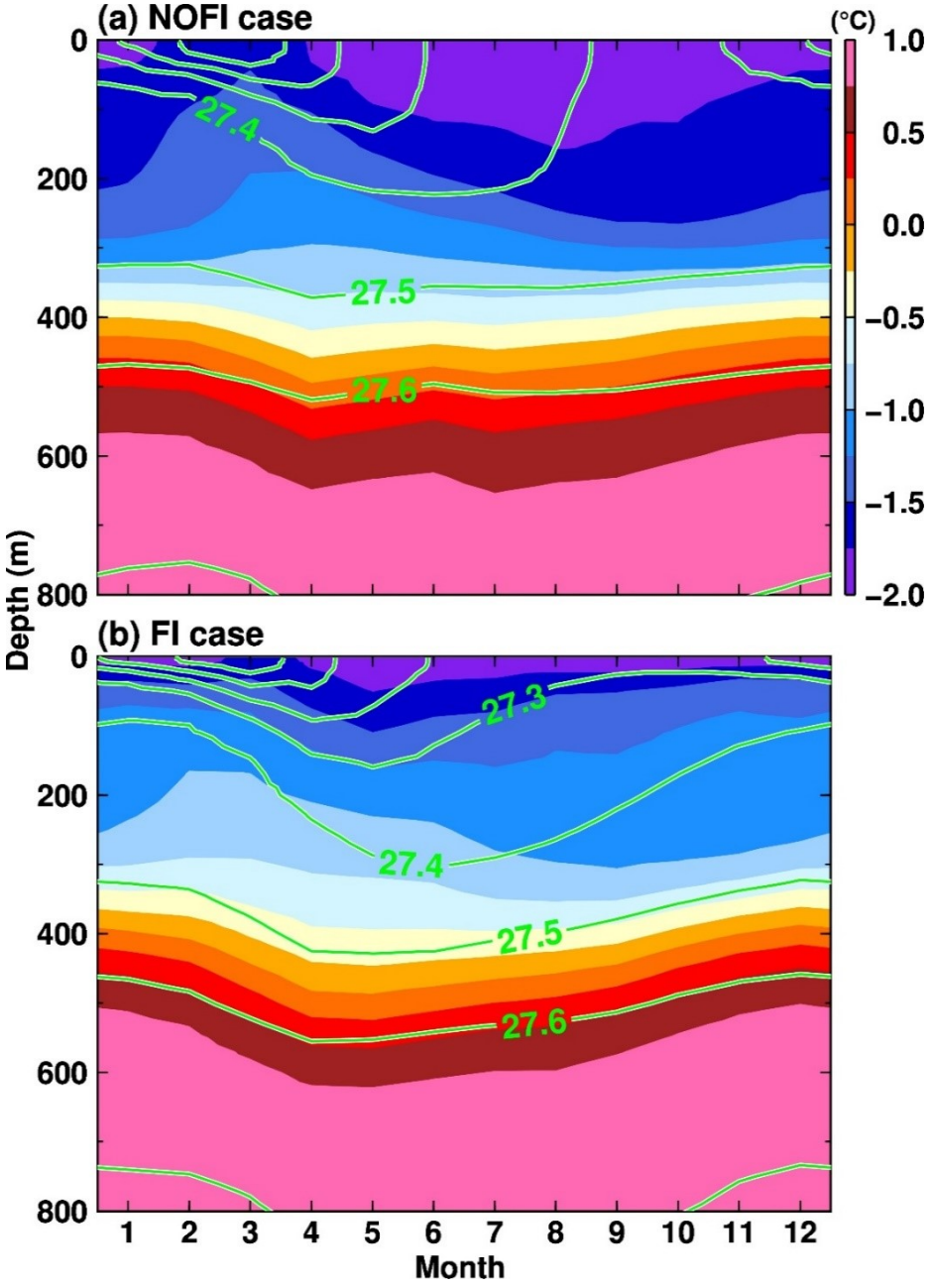

Figure 11: Seasonal variation of potential temperature (color) and potential density anomaly (green contours) averaged over the box area (Fig. 6) in the (a) NOFI and (b) FI cases. The variables were averaged over the period 2008-2018.

https://doi.org/10.5194/tc-2020-240
Preprint. Discussion started: 27 August 2020

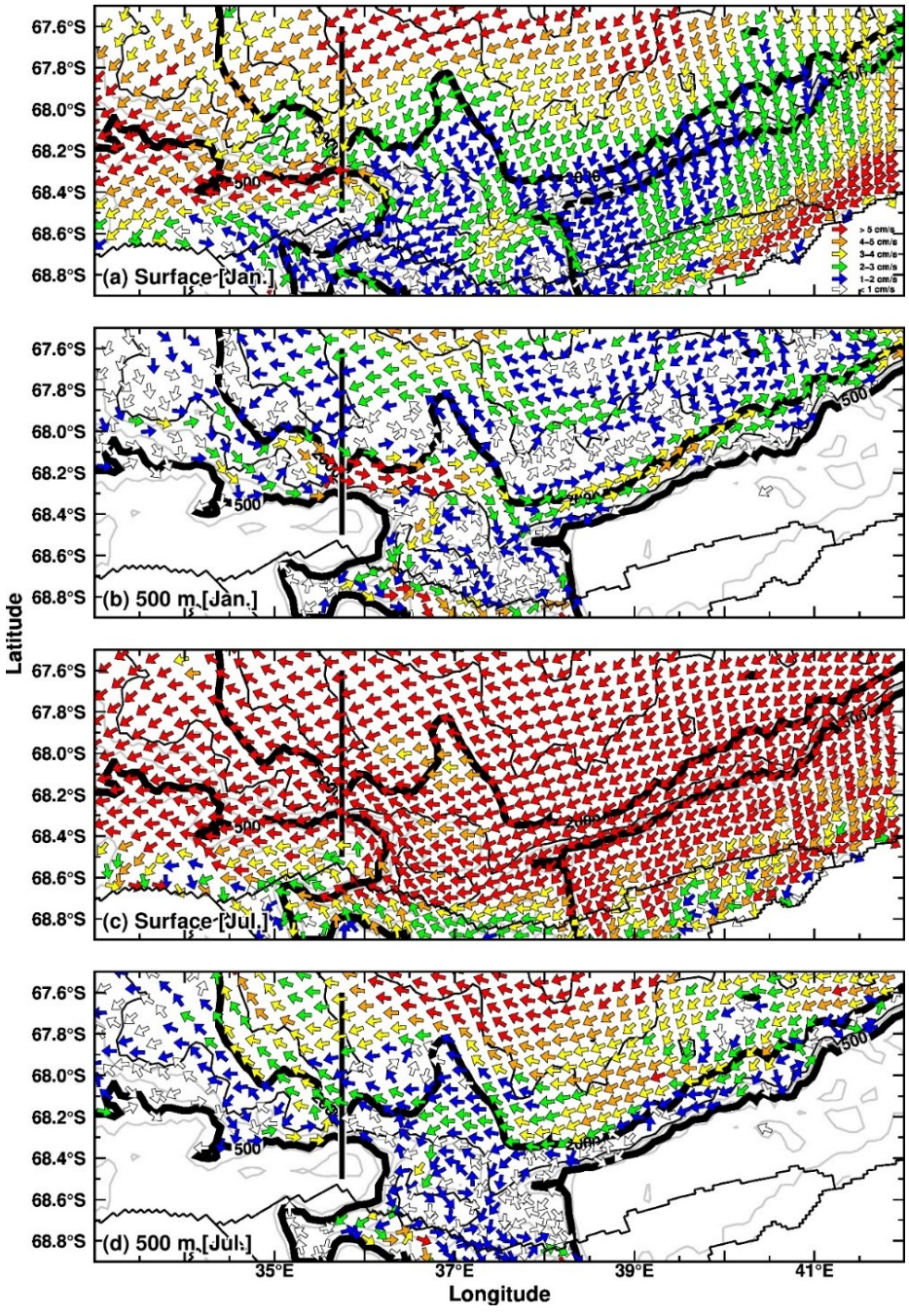

Figure 12: Maps of surface and intermediate-depth (at 500 m) ocean flows in (a-b) January and (c-d) July. The vector shows the ocean flow direction, and the color shows the magnitude. The vertical black line indicates the sections for Figure 13. The black contours show the water depth with the 1000-m interval. The thick black curves show the 500-m and 2000-m depth contours to represent the upper continental slope. The zigzag lines are coastline and the fast ice edge.

https://doi.org/10.5194/tc-2020-240
Preprint. Discussion started: 27 August 2020

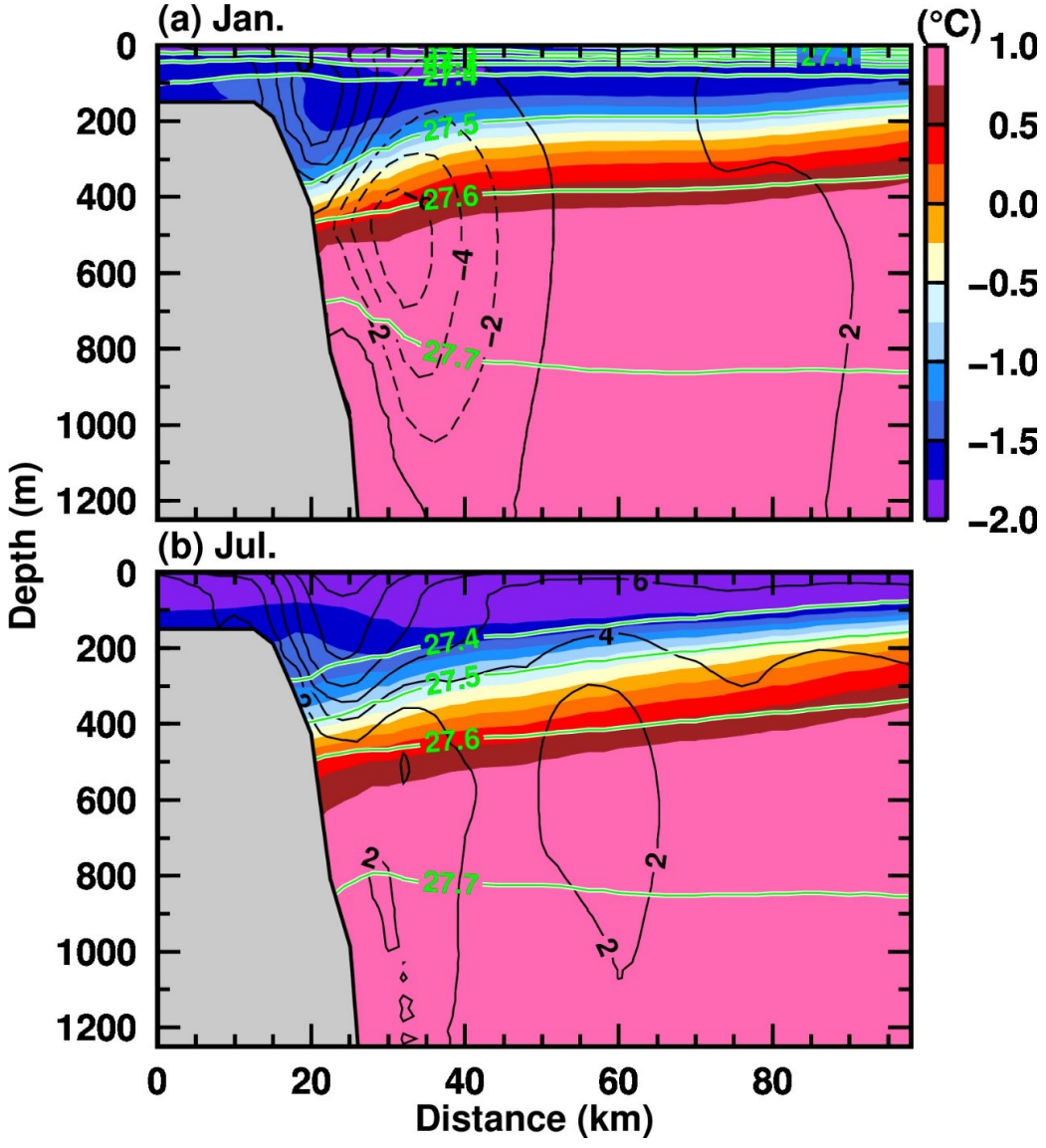

785 **Figure 13:** Vertical profiles of potential temperature (color), potential density anomaly (green contours), and west-eastward velocity (black contours) along the north-south section at 35.75°E in (a) January and (b) July. Positive and negative values in the velocity indicate westward and eastward, respectively. The variables were averaged over the period 2008-2018.

https://doi.org/10.5194/tc-2020-240
Preprint. Discussion started: 27 August 2020

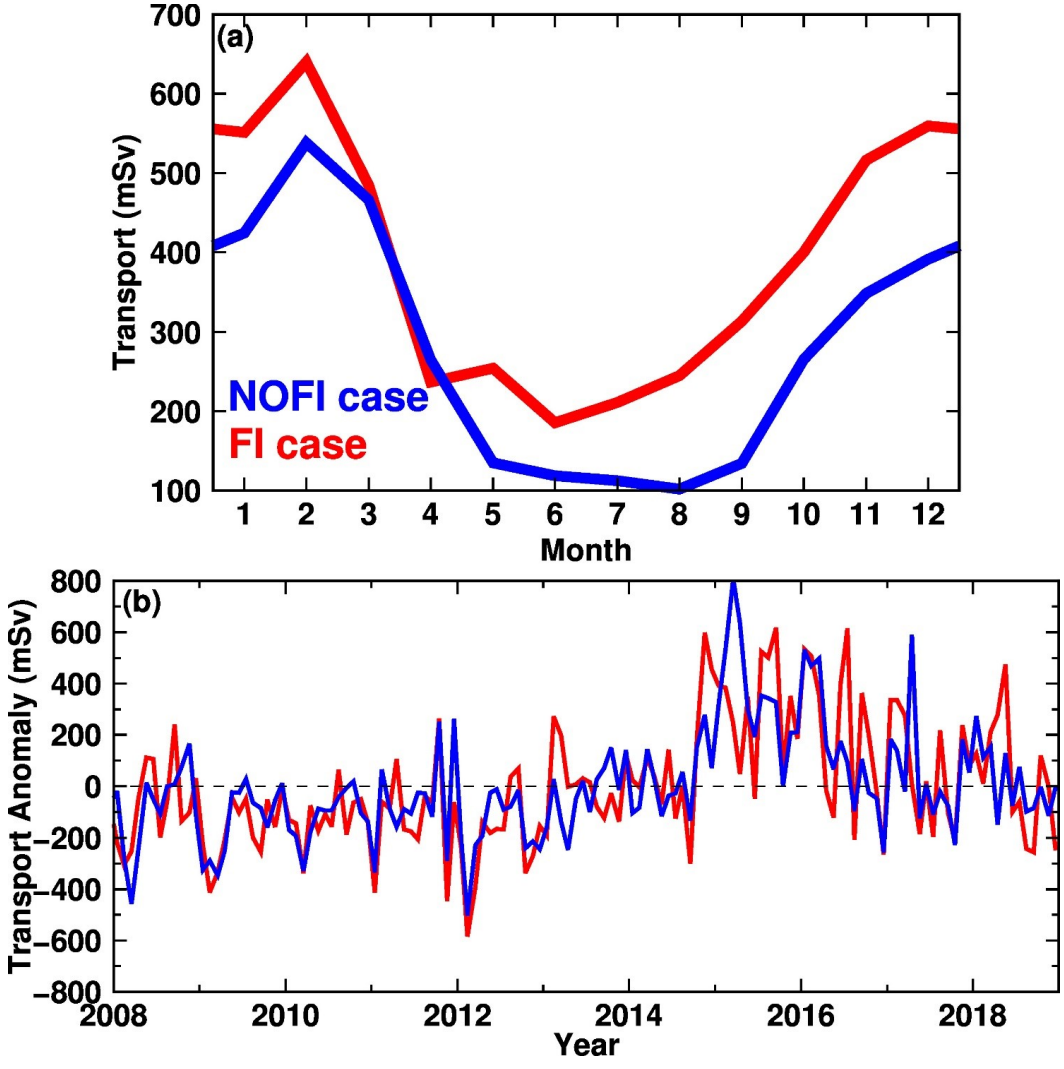

790 **Figure 14:** (a) Seasonal and (b) interannual variations of the eastward flow transport across the section at 35.75°E (see the black line in Fig. 12). The monthly transport in panel (a) is climatology averaged over the period 2008-2018. In panel (b), the interannual variation is shown by the anomaly from the monthly climatology

https://doi.org/10.5194/tc-2020-240
Preprint. Discussion started: 27 August 2020

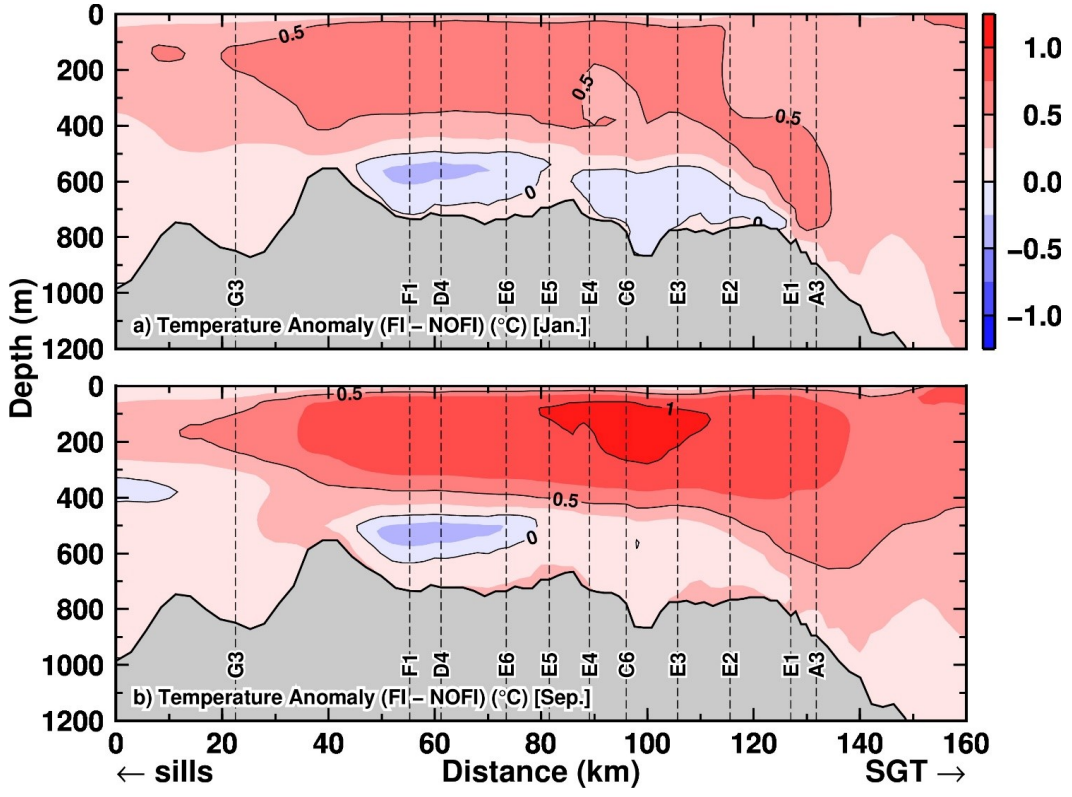

795 **Figure 15:** Vertical profiles of the temperature difference between the two cases (FI - NOFI) along the TROUGH section in (a) January and (b) September. The temperature difference calculated from the monthly mean climatologies averaged over the period 2008-2018. Vertical dashed lines indicate the observation stations in the section (see Fig. 6 for the locations).

https://doi.org/10.5194/tc-2020-240
Preprint. Discussion started: 27 August 2020

The Cryosphere
Discussions
Open Access
EGU

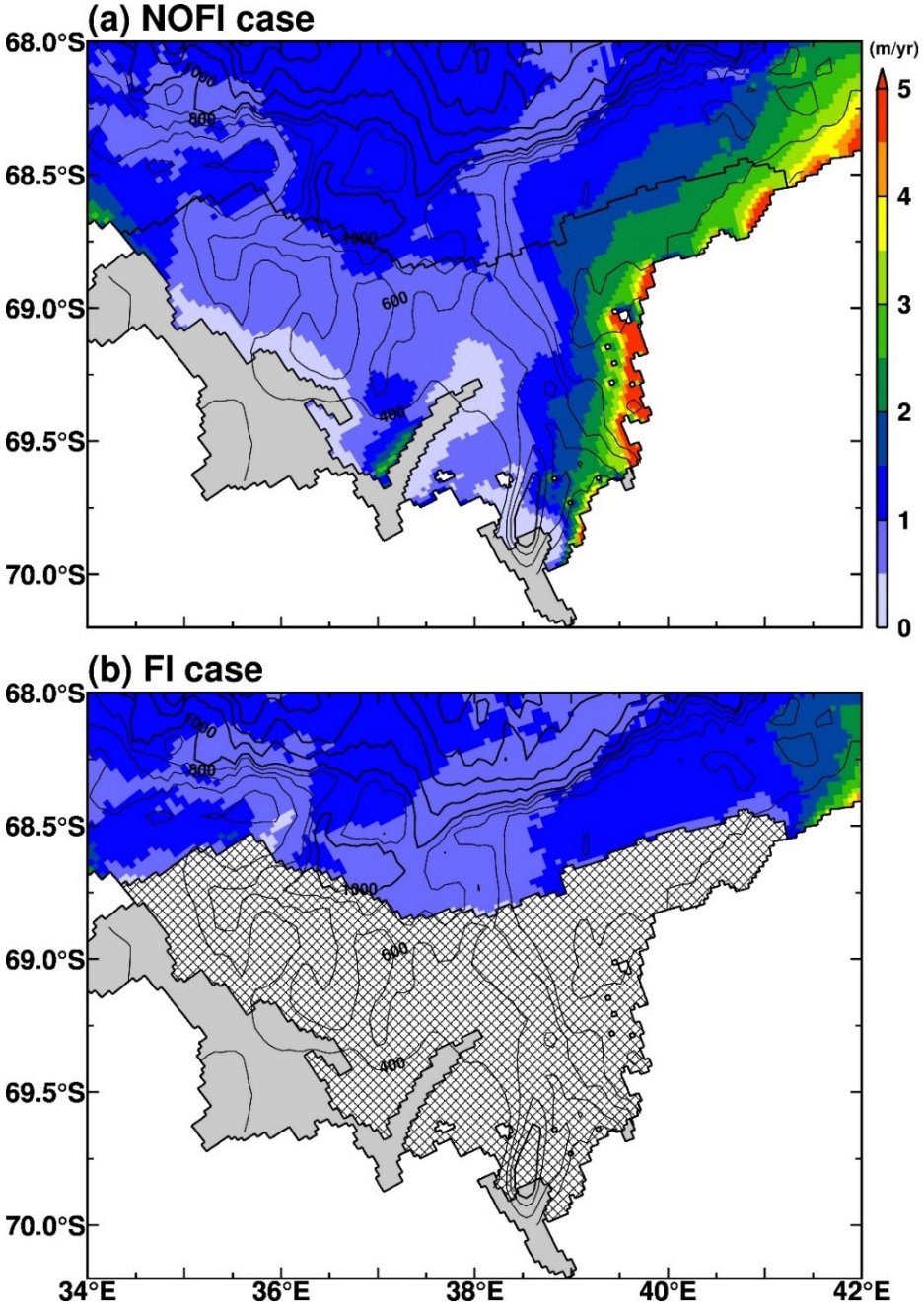

800 **Figure 16:** Maps of annual sea ice production (m yr^{-1}) in the (a) NOFI and (b) FI cases. The sea ice production was averaged over the period 2008-2018. The meshed region in the panel (b) indicates the fast ice cover. Gray shaded areas show ice shelves/glaciers. The contours show the water depth, with 200-m (1000-m) intervals in the regions shallower (deeper) than 1000 m.

https://doi.org/10.5194/tc-2020-240
Preprint. Discussion started: 27 August 2020

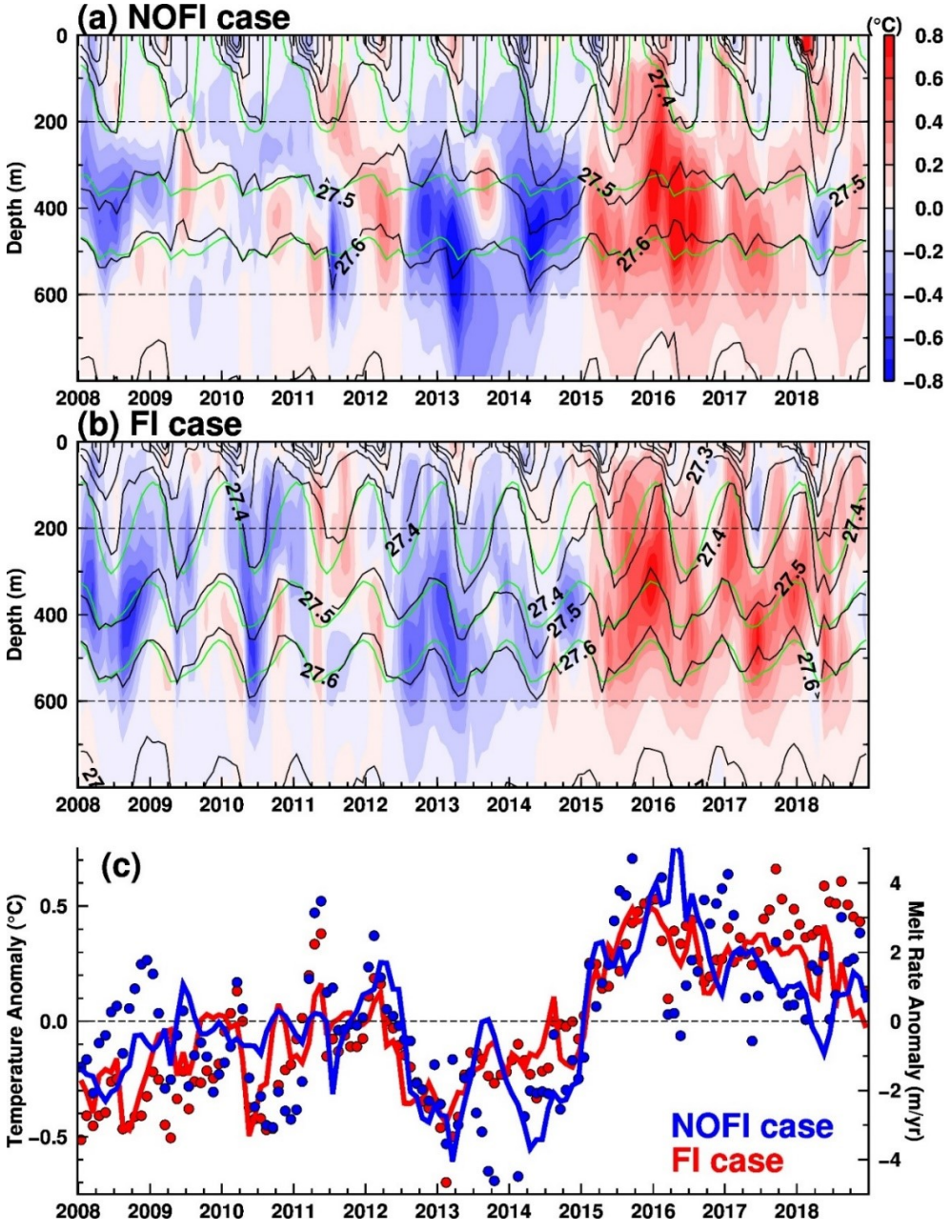

805

Figure 17: Time series of ocean temperature anomaly and potential density (a: vertical profile in the NOFI case, b: vertical profile in the FI case, and c: 200-600m averaged temperature) and the SGT melt rate anomaly (dots in the panel c). The anomalies are deviations from the monthly climatologies averaged over the period 2008-2018. Green curves in the panels a and b are climatologies of the potential density.

810

https://doi.org/10.5194/tc-2020-240
Preprint. Discussion started: 27 August 2020

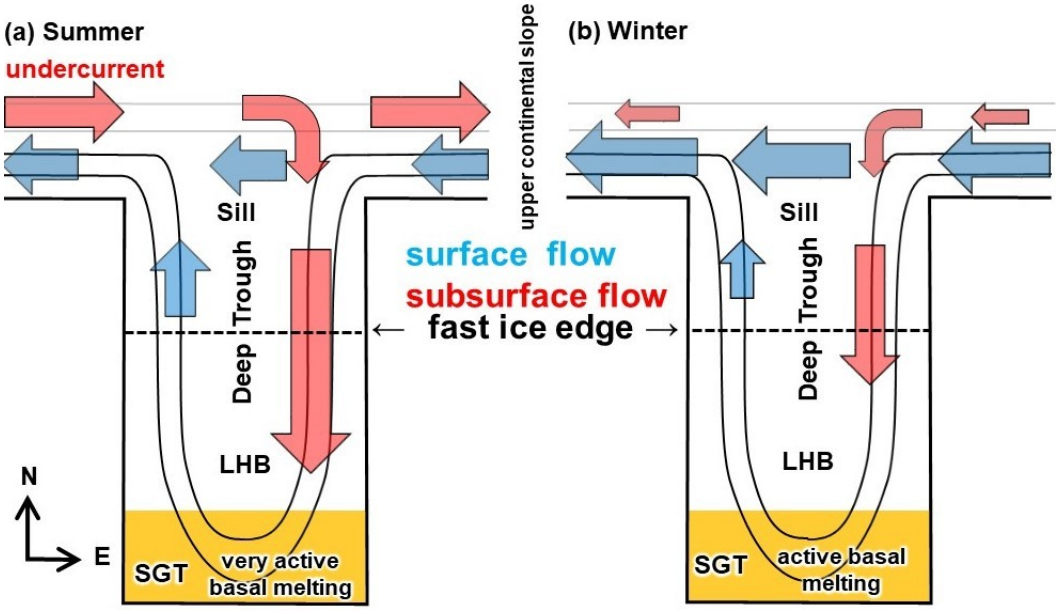

Figure 18: Schematic of ocean circulation in LHB in (a) summer and (b) winter. Blue and red arrows indicate ocean flows in the surface and subsurface/bottom layer, respectively. Black and grey lines show depth contours for the continental shelf and the upper continental slope regions, respectively. The dashed line is the edge of the fast ice.

815